How do ocean fronts structure pelagic ecosystems? A multi-sensor analysis in the Mozambique Channel.

A Thesis

submitted to

Indian Institute of Science Education and Research Pune in partial fulfilment of the requirements for the BS-MS Dual Degree Programme

by

Akash Dutta

Indian Institute of Science Education and Research Pune

Dr. Homi Bhabha Road,

Pashan, Pune 411008, INDIA.

April, 2024

Supervisor: Dr Vincent Rossi

Your Name: Akash Dutta

Certificate

This is to certify that this dissertation entitled

How do ocean fronts structure pelagic ecosystems? A multi-sensor analysis in the Mozambique Channel.

towards the partial fulfilment of the BS-MS dual degree programme at the Indian Institute of Science Education and Research, Pune represents study/work carried out by Akash Dutta at the Mediterranean Institute of Oceanography under the supervision of Dr Vincent Rossi, *Chargé de Recherche*, Equipe Océanographie Physique, Littorale et Côtière (OPLC), during the academic year 2023-2024.

Dr Vincent Rossi

Committee:

16/05/2024

Dr Vincent Rossi

Dr Joy Merwin Monteiro

This thesis is dedicated to
my dear grandparents,
the late Dipali (1944-2023) and Tapendu (1941-2024) Dutta
and to
the people of Gaza, Palestine,
who in facing very different kinds of death
have reminded me of the value of life.

Declaration

I hereby declare that the matter embodied in the report entitled "*How do ocean fronts structure pelagic ecosystems? A multi-sensor analysis in the Mozambique Channel.*" are the results of the work carried out by me at the Mediterranean Institute of Oceanography, Marseille, under the supervision of Dr. Vincent Rossi, and the same has not been submitted elsewhere for any other degree. Wherever others contribute, every effort is made to indicate this clearly, with due reference to the literature and acknowledgement of collaborative research and discussions.

Akash Dutta 

20191040

Table of Contents

List of Tables

List of Figures

Acknowledgements

This thesis would not have seen the light of day if not for the work, support and love of many people. I thank my supervisor, Vincent, for offering me this position, supporting me in adjusting to life at Marseille, advising and mentoring me throughout this project, and taking me fishing! Likewise Joy, my longtime mentor and expert evaluator of this thesis, has left a deep footprint on this work and on me generally; I owe to him much of my scientific competence and maturity. Thanks are due to Floriane, my colleague, on whose work I built and with whom I shared long lunches, wonderful books and two beautiful little hikes in the Calanques. The whole project depended on our funder, the program Ocean Front Change.

My family have pushed me to grow and yet held space for me to fall, with my parents responding to my concern with calm and my calm with concern. My grandparents have nourished me with comfort, laughter, good food and love. Abhav, Ankita and Prerna, the mainstays of my childhood, and my refuge in difficult times, are a part of me; my achievements are theirs.

At MIO, I was part of many rounds of *coinche* and trips to the *restaurant universitaire* with Marine, Nadege, Emma, Théo, Lauralie, Laurina, Hélène and Pierre, filling my days with good-natured fun and making good memories. It was a delight to have long evening phone calls with Arya, Vedant, Reetish, Spumpy, Anirban, Vasudha, Mausami, Ritvee, Manav, Sanjana, Manapat, Arsh, Soorya and occasionally Amogh Rakesh. Reetish, Spumpy and Soorya in particular actually helped me rethink specific analyses in my project.

Finally, I am proud to have the wonderful and irrepressible Tisha as my cousin sister, who knows better than anyone else how to make me laugh.

Abstract

In my project, I analysed 8 months' worth of Eulerian data (zooplankton, horizontal currents, temperature, salinity and pressure) from a multi-instrumented moored line deployed in 2022 in the central Mozambique Channel – a highly turbulent part of the world ocean prone to frontal activity. I synthesised this information with observations from satellites and from simulation outputs, to describe mesoscale and submesoscale ocean fronts in terms of the statistics of their occurrence, their depth profiles, and their interactions with living organisms. To do so, I defined a proxy for horizontal thermal gradients derived from mooring data, which I used to quantify frontal intensity at a length scale of tens of kilometres. I then verified prior results from model simulations regarding the depth profile of fronts. I show that in this dataset the subsurface gradient of temperature is poorly related to the SST gradient above it, a historically popular metric for fronts. Finally, I demonstrate clear impacts of enhanced thermal gradients on acoustic backscatter, used as a proxy for zooplankton.

Table on Notation

Symbol	Definition
ρ_0	Boussinesq (mean) density of the ocean
p	Pressure
ρ	Density
T	Temperature
S	Salinity
u, v, w	Velocity components along x, y, z-axes respectively
$\mathbf{u}$	Velocity as a vector
$\hat{\mathbf{u}}$	Unit vector in the direction of the current velocity
f	Coriolis frequency
g	Acceleration due to gravity
$\mathcal{U}$	Scale of the horizontal velocity
$\mathcal{L}$	Length scale of interest
Ro	Rossby number, given by $f\,\mathcal{U}/\mathcal{L}$
$\mathbf{u_g}, \mathbf{u_a}$	Geostrophic and ageostrophic velocities
$\nabla \mathbf{T}_h$	Horizontal temperature gradient; the subscript h is usually understood
$\nabla T_{\|\|}$	The "alongcurrent" component of the gradient of temperature (§ 2.3)
S_v	Volumetric scattering coefficient/acoustic backscatter
N	Brunt-Väisälä frequency; its square is the stratification
$\mathcal{L}_d$	Rossby deformation radius

Introduction

1.1 The dynamics of ocean fronts

The global ocean circulation is a superposition of currents over an extensive range of length and time scales. At large scales ($\sim 1000\ \mathrm{km}, 1\ \mathrm{yr}$), the ocean is forced by inputs of heat, salinity and momentum (via wind-stress) to produce a system of gyres and currents. Superimposed on this flow is an equally energetic mesoscale eddy field ($\sim 100\ \mathrm{km}, 1\ \mathrm{month}$), which is driven by internal instabilities of the mean flow as well as by more local forcings. The powerful *geostrophic approximation*—that variations in pressure are balanced by the Coriolis force—is valid for horizontal currents at both of these scales (Vallis, 2005). Decomposing the velocity and pressure fields into a geostrophic and ageostrophic component, $\mathbf{u} = \mathbf{u}_g + \mathbf{u}_a\ ;\ P = P_g + P_a$, where the ageostrophic components are smaller by a factor of the Rossby number (Ro). Then:

$$f\,\mathbf{k} \times \mathbf{u}_g = -\frac{\nabla \mathbf{P}_g}{\rho_0}$$

Thus the geostrophic flow is everywhere tangential to contours of pressure, and on an f-plane is thus nondivergent and horizontal to leading order. All vertical motion in the ocean is thus due to the divergence of *ageostrophic velocities* $(\nabla \cdot \mathbf{u}_a)$. However, the persistent action of *fine submesoscale* (time period: hours to days) inertia-gravity waves (IGWs) (Vanneste, 2013) carry deviations from geostrophy away to the basin boundaries; they keep the Rossby number small at all longer timescales. This means that the vertical motion, too, is usually negligible at large scales. It can be forced, as in the Ekman pumping in gyres; and of course we see it at coastal boundaries. But there is a third possibility: dynamical features at the submesoscale, which are short-lived enough to see the build-up of considerable ageostrophic momenta. An example of such a feature is the submesoscale ocean front, with a width on the order of 0.1 to $10\ \mathrm{km}$, and a timescale ranging from a few hours to a couple of weeks. (McWilliams, 2016)

A front is a narrow region of enhanced tracer gradients. It is usually produced by a strongly sheared *confluent flow pattern* as illustrated in *Fig 1*, where the tracer of interest is density. (This is hereafter called a *density* front). Such patterns are often found at the boundary of two eddies in contact. The flow is, to leading order, geostrophic, and the sloping isopycnals illustrated below the surface produce a pressure gradient which is in balance with these currents. At this stage we make three observations: (McWilliams, 2016; Hoskins, 1982)

1. The inflow of water along the x-axis contracts the length scale over which density (or any other tracer, like chlorophyll) varies. This acts to sharpen the tracer *gradient* along x, a process called **frontogenesis.**(Hoskins, 1982)
2. Due to their inertia, the currents approaching the front maintain their momentum along x. To maintain geostrophic balance, they must be deflected by some mechanism along the y-axis. If the deflection is insufficient, the confluent character of the circulation increases with time and frontogenesis continues.
3. The inflow of positively/negatively buoyant water on the light/heavy side of the front should induce *vertical velocities* as the water "climbs" along the isopycnal slopes. This is termed a restratifying buoyancy flux. Here too, if this vertical velocity is insufficient, the slope continues to steepen and and thus strengthens the front.

In fact, points 2 and 3 are mechanistically related. The deflection of the geostrophic current is due to the Coriolis effect resulting from the ageostrophic component. In terms of a vorticity budget, we can see that ageostrophic divergence/convergence (marked D/C respectively in Fig. 1.1) can cause the geostrophic

currents to turn aside. The same divergence, denoted $\nabla \cdot \mathbf{u}_a$ also drives the vertical circulation in point 3, and thus acts as a feedback of the ageostrophic circulation on the geostrophic fields. In theory, the front will sharpen until this feedback arrests the process.

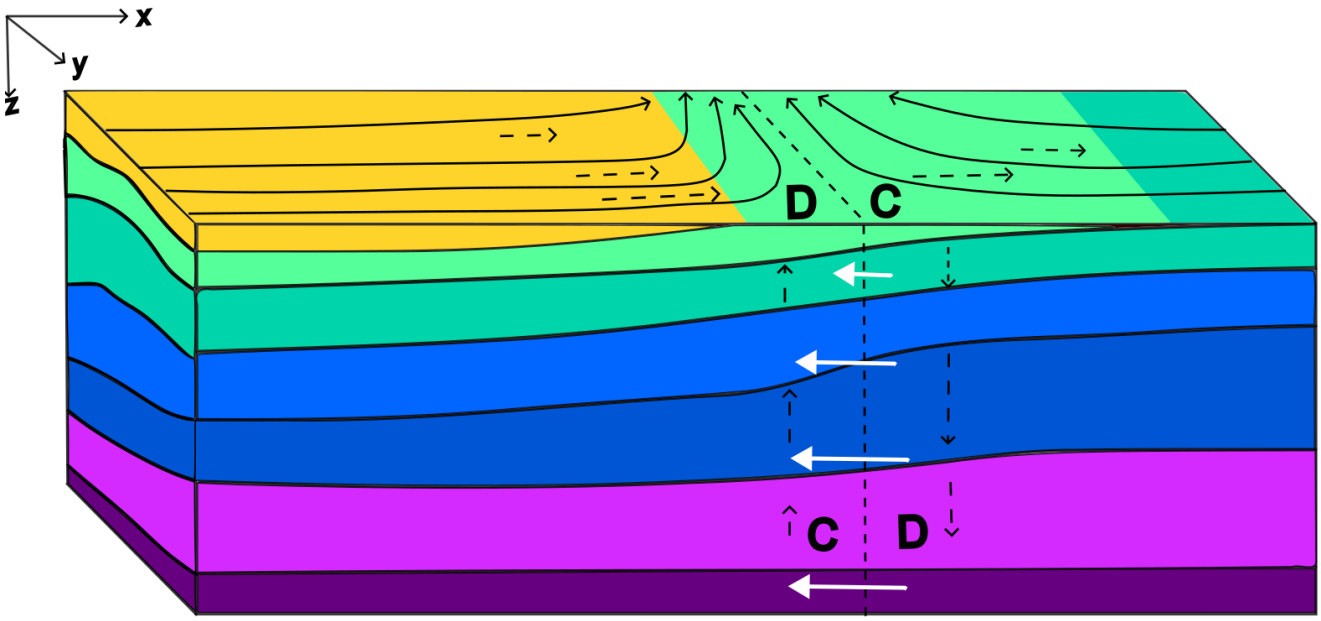

Figure 1.1: In the frame of reference co-moving with the front (with a corresponding portion of the isopycnal slope removed). Sloping isopycnal layers are illustrated in different colours, with outcropping layers at the surface visible to satellites. $\nabla_{\mathbf{h}}\mathbf{P}$ is illustrated in white arrows; the geostrophic circulation in solid black arrows on the upper face; ageostrophic circulation in the x-z plane in dashed arrows (y-component not shown); and convergent/divergent zones are marked C/D respectively

We cannot *a priori* constrain the behaviour of this term $\nabla \cdot \mathbf{u}_a$, but over long timescales, the result of its feedback on ρ and $\mathbf{u_g}$ must be to maintain the geostrophic relation between them. This constraint is exploited by the elegant *quasi-geostrophic model*[1] of frontogenesis, developed by meteorologists to get a predictive model of the evolution of fronts. This model arrests the frontogenic process at around the Rossby radius of deformation (Hoskins, 1982) (~ 200 km at the equator but 10 km at the poles; about $20-25$km in the Mozambique Channel according to Vassele, accessed at https://hdl.handle.net/1956/7013).

However, this model excludes the direct effect of the ageostrophic convergence on the frontal width, deeming it negligible (of order Ro). This phenomenon serves to further contract the cross-front length scale in the zones marked C, while de-intensifying frontogenesis in the zones marked D. As the front sharpens, Ro increases and this second correction becomes more and more pronounced, ruling out a simple balanced state. This effect was first described by Hoskins (1982), and provides for *super-exponential* frontogenesis. The width contracts until the front is at submesoscale length scales, where $Ro \sim \mathcal{O}(1)$ and ageostrophic convergence can generate strong vertical currents of up to 100 m/day in some numerical simulations(Mahadevan et al., 2006). This is particularly enhanced in the relatively unstratified mixed layer.

While the mechanism detailed above relies on buoyancy effects and thus density gradients, other types of fronts than density fronts exist. Mechanisms such as wind-stress, or flow from the boundaries, too, can create confluent flow regimes that advect material into a narrow region with a strong shear. (McWilliam, 2016)

Note that confluence need not imply local convergence ($\nabla \cdot \mathbf{u} < 0$) of the horizontal flow. The confluent character of the flow field can be quantified by the finite-size Lyapunov exponents (FSLEs) of the flow field

(Samelson, 2013). Confluent flow in general can also shape ecosystems, in a manner independent of vertical pumping: via the passive aggregation of plankton species facilitating community interactions; or alternatively, acting as a barrier between different ecosystems this mechanism is independent of vertical circulation. (Lévy et al., 2018)

Moreover, other mechanisms such as mixed-layer instabilities, topographic forcing, or local Ekman pumping, can produce submesoscale density fronts without mesoscale confluent flow. They induce vertical velocities directly, and non-uniformly over a horizontal extent, leading to sloping isopycnals and thus frontogenesis (McWilliams, 2016). Sloping isopycnals in the surface boundary layer are likely to either undergo restratification, and subside below the mixed layer; or to be caught up in wind-driven mixing and homogenisation. However, while these processes tend to reduce differences in ρ, they are indifferent to variations in temperature (T) and salinity (S) *along* isopycnal surfaces. This has the important consequence for gradients of *sea surface temperature* (SST), often used as a proxy for surface density fronts; these may include *density-compensated fronts,* (Chin et al., 1995) with which a vertical circulation is not associated. These may be disambiguated by referring to measurements of sea surface *salinity* (SSS); but the resolution on these datasets is presently poorer than that of SST and often insufficient to fully resolve the submesoscale.

1.2 The biological importance of ocean fronts

Observations of biological activity localised at fronts are legion. The largest body of work concerns the use of *sea surface temperature* gradients $|\nabla T|_s$, derived from satellite imaging as a proxy for fronts at the surface. These fronts have been co-localised with anomalously high concentrations of organisms in the literature—using satellite-derived chlorophyll concentrations (denoted chl) for phytoplankton and ship-based observations for phytoplankton, zooplankton and fish. Another metric for surface fronts relies on long timeseries of satellite observations of a surface flow field (geostrophic plus Ekman velocities), which allow us to calculate FSLEs for the timescale of interest. Confluent (and interestingly, diffluent) flow regimes have both been correlated with activity at various trophic levels, including preferential foraging by top predators like frigate birds. (Tew-Kai et al., 2009) Nevertheless, counterexamples of these patterns exist as well; see fig 1.2 for an example.

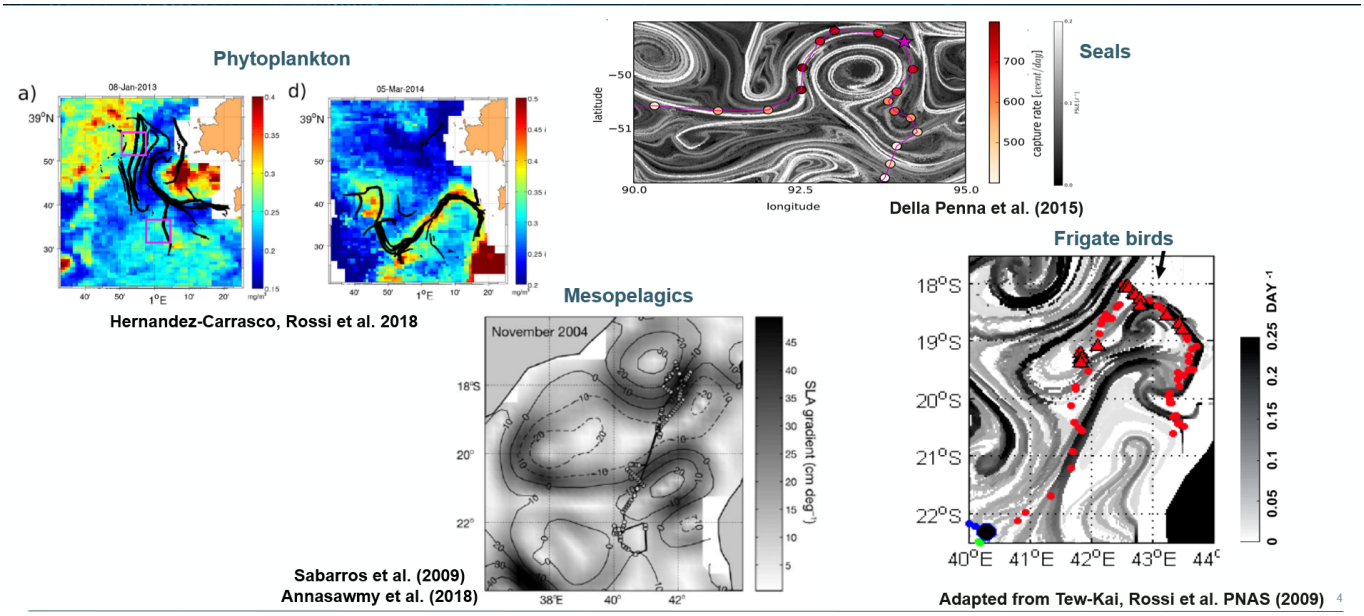

Fig 1.2: Adapted figures from existing literature showing associations—both positive (d) and negative (a)—

between phytoplankton and density fronts (Hernandez-Carrasco et al., 2018); between encounters with mesopelagics and gradients of sea level anomaly (Sabarros et al., 2009, Annasawmy et al., 2018); and between elephant seal (Della Penna et al., 2015) as well as frigate bird (Tew-Kai et al., 2009) tracks and FSLEs

Oceanographic cruises have undertaken front transects (traversing a front multiple times in the cross-front direction) to measure profiles of all oceanographic variables; the fronts are often located using SST gradients. Biological taxa abundances can be broadly classified into those that *peak* at the front, and those that *transition* from one steady value to another upon crossing the front. If a given front displays a pattern consistent across taxa, it is characterised as a "peak" or "transition" front; and while transition fronts are to be expected if the taxa on either side of the front are modelled as passive tracers, the existence of peak fronts hints at biologically active mechanisms. Competitive and predatory interactions between these taxa have been identified as candidate mechanisms, as have the impacts of vertical motion discussed above (Lévy et al., 2018). Of note is that competition and predation can suppress a chlorophyll signal even at a biologically active peak front, explaining some of the variance between $|\nabla T|_s$ and $|\nabla chl|_s$.

Fronts are thus of biological relevance, but historically understood in a surface-limited perspective. Over the last three decades there has been increasing theoretical and observational evidence for deep (up to $1\ \mathrm{km}$) submesoscale activity. Work by my colleagues (Sudre et al, 2023a) investigated fronts at depth through numerical modelling of the physics of the Mozambique Channel, which was chosen as an ideal setting given its high turbulence, current variability and mesoscale eddy kinetic energy. It supports a rich ecosystem whose sustainable usage requires an understanding of the drivers of biological productivity.

The study used nested regional ocean models to study vertical profiles of thermal gradients in four different meridional ranges of the Mozambique channel, and to link these to mesoscale strain and topography. The study found that the most intense thermal gradients were at the base of the mixed layer, at the subsurface pycnocline ($z \sim 80 - 100$m), as well as a seasonal cycle in the frontal signature (peaking in Jul-Sep and again in Dec-Feb). Note that the focus was on thermal rather than density fronts, owing to the fact that the freshwater load from the Zambezi river is not represented in the model, introducing local errors in salinity and thus density near the coast.

My thesis investigates fronts across a range of depths from *in situ* data, derived from a mooring. The mooring was placed on a seamount in the South Moxambique Channel. The placement was opportunistic, as the location was along a cruise track. Mooring-based sensors recorded timeseries of temperature and current velocity over an 8-month period (27/04/2022-12/12/2022). Current measurements were taken by an Acoustic Doppler Current Profiler, from whose measurements of raw echo strength can be inferred a profile of *acoustic backscatter*, which serves as a proxy of relative zooplankton abundance.

I introduce a proxy for thermal gradients based on the passive transport of temperature, and validate it against model results. I then attempt to explore the depth structure of thermal fronts at the mooring location, to examine whether it is coherent with Sudre et al's predictions. I also accessed satellite data (MetOp) to examine fronts from SST, and to examine correlations with gradients at depth. Further, I analyse the relationship between acoustic backscatter and frontal intensity across depths, in the light of the vertical migration of zooplankton populations. This study thus allows for the comparison of three different approaches $-$model, mooring and satellite$-$to study the same physical phenomenon, as well as its ecological ramifications.

The study is limited by its lack of a direct measurement of thermal gradients, as well as the lack of a salinity profile allowing the calculation of density gradients. Using the ADCPs tend to produce noisy measurements of the vertical velocity, which reduces our ability to quantify the impact of vertical motions on productivity. Data on chlorophyll, fish and marine mammals are unfortunately unavailable in the present set-up owing to equipment failure.

The present study focusses on providing a quantitative, coherent *description* of thermal fronts and their impact on zooplankton abundances. It does not, thus, make of use of the tools of inferential statistics, such as confidence intervals or p-values, to contrast different candidate mechanisms and identify which one is supported by the data. That kind of work would require a pre-existing understanding of the probability distributions according to different models, of the variables sampled in this study. Therefore I restrict myself to the tools of *descriptive statistics*, like (bootstrapped) correlation coefficients, means and standard deviations. By examining these quantities, I present a set of possible, internally consistent, interpretations and discuss them in light of the literature. I do not make any claims as to the *generalisability* of my conclusions to other datasets.

Materials and Methods

2.1 Mooring deployment and data

The mooring was deployed in the Southern Mozambique channel on 25/04/2022; its position in the channel was opportunistic (along the cruise track). The final choice of location was the northern flank of the Jaguar seamount at depth $\sim 1\ \mathrm{km}$ with a flat top was chosen, to sample only the upper water column and to ensure small drift during deployment would not result in large depth deviations. The coordinates were: $21^{\circ}44.7833'\ \mathrm{S} 39^{\circ}32.4553'\ \mathrm{E}$ at a depth of $1054\ m$, near the *Bassas da India* atoll.

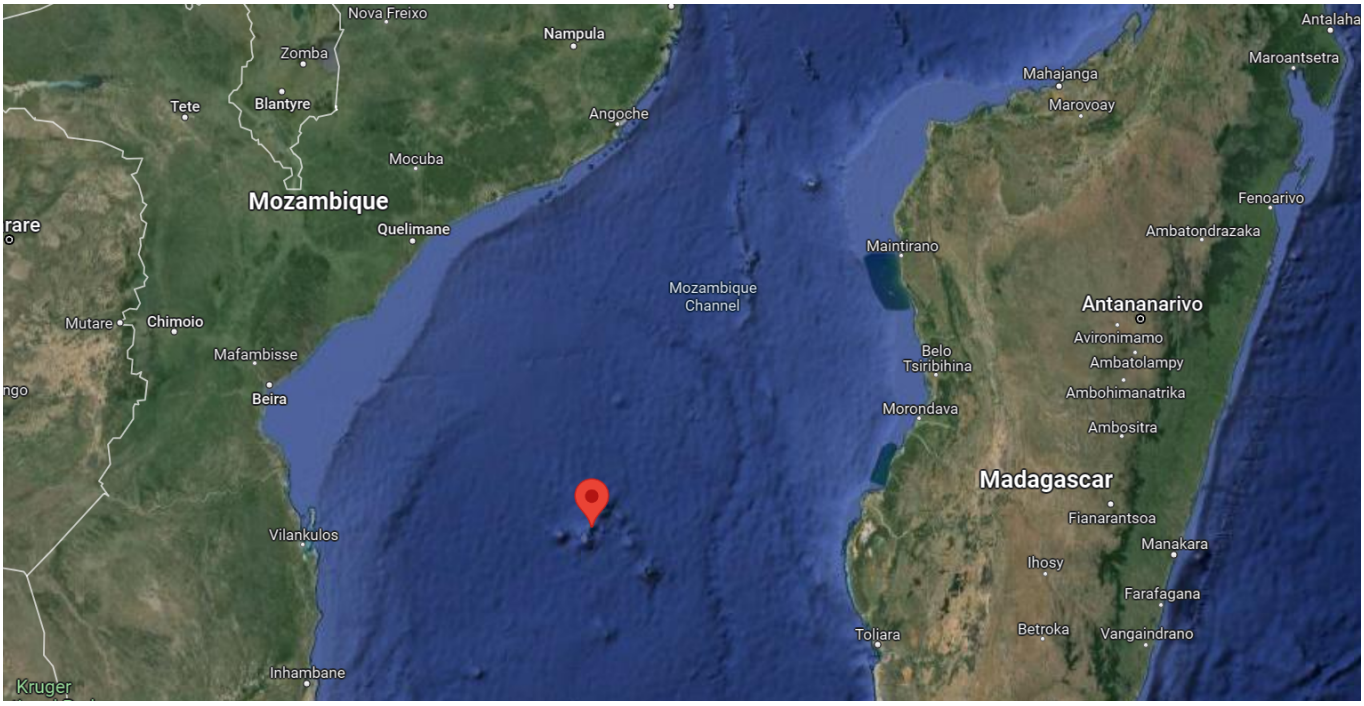

Fig 2.1: Mooring location

A summary of the instruments are provided in Table 2.1 and Fig 2.1. The array of temperature detectors are concentrated in the mixed layer and thermocline, as well as near and in the Bottom Boundary Layer (BBL). The pair of ADCPs, oriented upward and downward and mounted on a common rosette, measure a profile of current velocities $u,\ v,\ w$ and an echo intensity I, across a depth range of roughly $0 - 200\ \mathrm{m}$. The instrument divides the water column into 5-meter-deep cells and records a value of each variable from each cell. Note the failure of the SBE39+ at 600m, the fluorometer, and the hydrophones. Critically, we lose the information on phytoplankton abundances (chlorophyll) and the passing of larger organisms such as cetaceans (the hydrophones). The profile of temperature is also affected by a loss of one measurement.

Table 2.1: Instruments and Observations

Instrument	Variable Measured	Target Depth	Functioned?	Nominal depth of data
CTD(SBE37)	Temperature, Salinity	40m	Yes	25m
SBE39	Temperature	110m, 150m, 300m, 800m, 900m, 1039m	Yes	95m, 135m, 285m, uncertain, uncertain, uncertain
SBE39+	Temperature, Pressure	62m, 200m, 400m, 600m	Yes, except at 600m	Respectively: 48m, 185, 337m, N/A
Rosette bearing 2 ADCPs	Profiles of current velocities and acoustic backscatter	80m	Yes	65m
Fluorometer	Chlorophyll concentration (phytoplankton)	40m	No	No data
Hydrophones	Presence/absence of marine mammals (esp. cetaceans)	96m-104m	No	No data

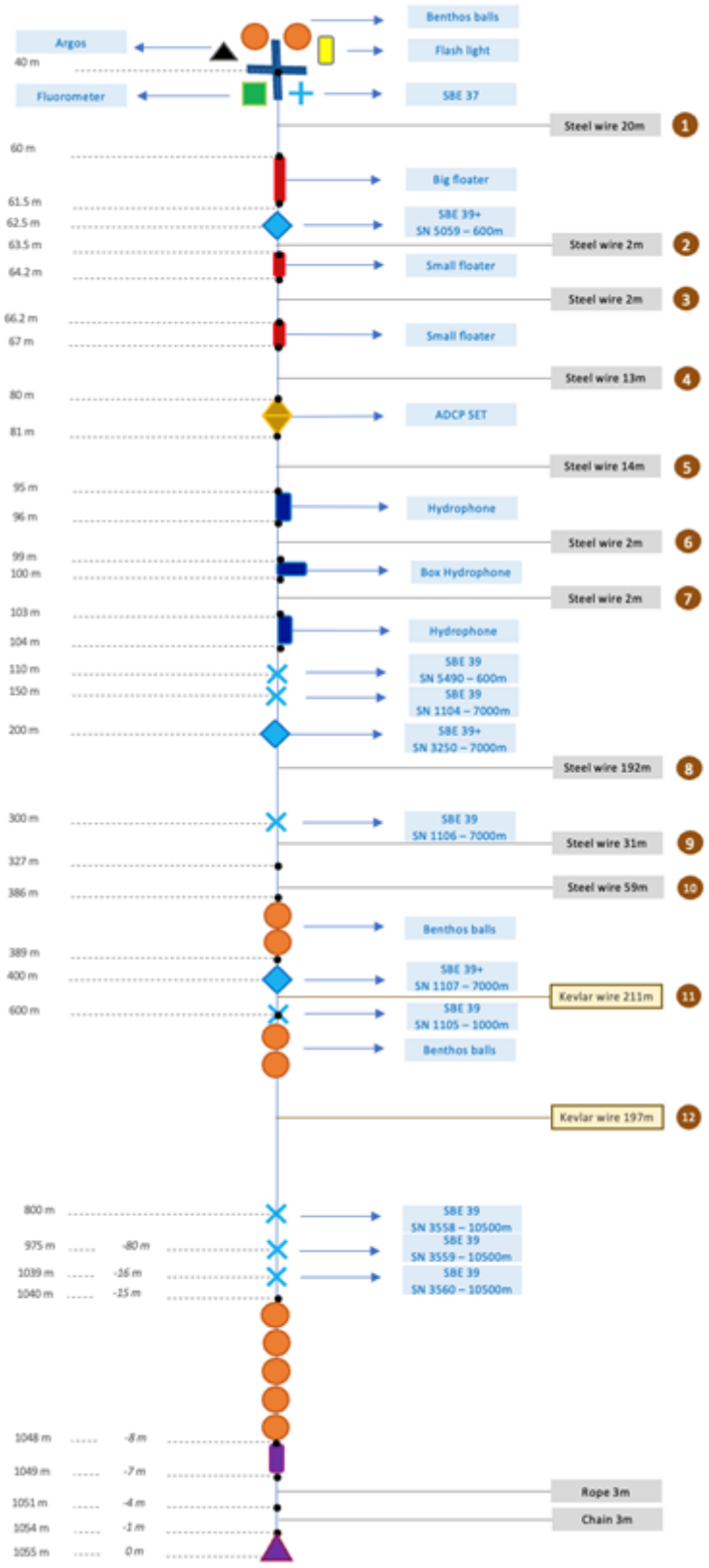

Figure 2.2: Schematic of the mooring as planned for deployment prior to the mission

The real-time depths of each instrument are calculated using the SBE39+ pressure measurements, by equating pressure in decibars to depth in meters. The mooring bends due to horizontal currents, and the real-time depths thus fluctuate. By modelling the mooring as made of rigid linear segments of known length between successive pressure detectors, depths of intermediate sensors are deduced from the angle of such

a segment with the vertical. Ideally, the minimum depths (i.e., erect mooring) of each instrument match the target depths.

Instead, a mismatch is observed. The instruments targeted to 40, 62 and $200\mathrm{m}$ have minimum depths of 25, 48 and $185\mathrm{m}$ respectively, while the one targeted to $400\mathrm{m}$ was found instead at $360\mathrm{m}$! This allows us to ascribe nominal depths to all instruments above $200\ \mathrm{m}$, with an upward deviation of $15\ \mathrm{m}$. With the failure of the $600\ \mathrm{m}$ sensor, it is unknown if the near-bottom instruments were also shifted up by $60\ \mathrm{m}$, or if that was peculiar to a single instrument. These data were not exploited in this project, rendering the point moot. The nominal depth of the sensor targeted to $300\ \mathrm{m}$ remains in question—it could be $285\ \mathrm{m}$ or $240\ \mathrm{m}$. A cubic splines interpolation of temperature measured by the other sensors fits better with the sensor at $285\ \mathrm{m}$, which was thus designated the nominal depth.

The data for T were recorded every 15 minutes, while those for u, v, w and I were at an hourly frequency. The ADCP data included some spurious observations which had to be discarded. These were from:

- the cells immediately neighbouring the instrument, echoes from which tend to be contaminated by the ADCP's own noise;
- the second cell above the rosette, whose receptor ("range gate") was defective;
- values from near the surface (in our case the top $11\ \mathrm{m}$), contaminated by a loud sidelobe reflection(Lentz et al., 2022); and,
- values with poor quality flags (percent good < 80 or error velocity > 5 m/s) (Gordon, 1996)

Profiles of $T,\ u,\ v$ and w were then interpolated onto a vertical grid of $5\ \mathrm{m}$ spacing from the surface downwards using cubic splines from `scipy.interpolate`. The temperature profile of only the "shallow" depths (till the $340\ \mathrm{m}$ SBE39) was nearly linear except for a spurious kink near the bottom; hence it was re-interpolated linearly.

Scatterer abundance is another variable of interest, as the scatterers include zooplankton and micronekton. Higher abundances at a depth correlate to stronger echoes from that depth; by correcting the raw echo intensity for effects such as beam spreading, and attenuation of sound by water and dissolved solutes, we can extract an **acoustic backscatter coefficient** S_v. This was done following Deines, 1999, using expressions for beam attenuation from Francois and Garrison, 1982 (Figure 7). Attenuation was calculated for representative values of **ocean salinity=35** and **pH=8**. (Attenuation due to $\mathrm{MgSO_4}$ varies significantly only over a salinity range of $30 - 35$(Francois et al., 1982); while the CTD always registered salinity values between 35 and 35.5). While the power of the battery was assumed (Deines, 1999) at a representative value of $33\ \mathrm{V}$, the actual power of the real battery was not available to me. It is immaterial, however, as the data are used as a *relative* proxy of scatterer abundance. We cannot, from these data, identify different zooplankton taxa, nor calculate biomass values, as we lack a calibration against dry-weight biomass. (Flagg et al., 1989)

These data were calculated from the values of I without interpolation, for each 5-meter cell. Consequently, there are no data for S_v from the discarded cells—namely the near-surface and near-instrument ones. These data were subsequently re-gridded on a standard grid. (Example: if a cell had a depth range of $14.37 - 19.37\ \mathrm{m}$, its value of S_v is attributed an index of $15\ \mathrm{m}$.)

2.2 A proxy for thermal gradients.

Suppose a front passes by the mooring. Then at every depth z, we have a timeseries of temperature $T(t)$ from which we can approximate $\partial T/\partial t$ by a centred difference: $\left(\frac{\partial T}{\partial t} \approx \frac{T(z,t+1)-T(z,t-1)}{2}\right)$. Large values of this quantity would intuitively stand in for the passage of intense gradients. We require an expression in terms of $\partial T/\partial t$ as an estimate of $|\nabla_{\mathbf{h}}\mathbf{T}|$ with units of $\mathrm{K\ km^{-1}}$.

Consider the conservative temperature evolution equation, including advection and forcing terms:

$$\frac{\partial \Theta}{\partial t} + \mathbf{u_h} \cdot \nabla_{\mathbf{h}} \mathbf{\Theta} + w\frac{\partial \Theta}{\partial z} = \mathfrak{F}(\Theta)$$

where $\mathfrak{F}(\Theta)$ denotes the nonconservative *forcing* of Θ, i.e., diabatic heat flux. Expressing Θ as $\Theta(T, z)$ and suppressing the subscript h, we get:

$$\frac{\partial T}{\partial t} + \mathbf{u} \cdot \nabla \mathbf{T} = \left(\frac{\partial \Theta}{\partial T}\right)^{-1} \left(\mathfrak{F}(\Theta) - w\frac{\partial \Theta}{\partial z}\right)$$

First, we assert that the right-hand side terms can be neglected. The diabatic forcing can be scaled by assuming that incoming radiation is distributed over the whole mixed layer of depth $\sim 100\ \mathrm{m}$. Starting with established scales for incoming radiation (Wild et al., 2015) and scaling both the density and specific heat of seawater as 10^3 in SI units:

$$10^2\ -\ 10^3\ \mathrm{W\ m^{-2}\ day^{-1}} \implies 10^{-2}\ \mathrm{K\ day^{-1}}.$$

Which is very small compared observed values of $\partial T/\partial t$ in the range of $1\ \mathrm{K\ day^{-1}}$.

Very strong vertical velocities cannot be ruled out *a priori* at the submesoscale, and an upward movement of a few tens of meters in a day would be a strong source of error in the calculations. Robust measurements of w were not available to us from the ADCP data (as the measured values include active vertical motion by biotic scatterers), but previous measurements invoking quasi-geostrophy and the omega equation (Comby et al., 2022) indicate a range of 4 to $40\ \mathrm{m\ day^{-1}}$. However, the Lagrangian trajectories of those water parcels are usually oscillatory in depth, tending to restore a water parcel to its depth of origin (Vélez Blechí et al., 2001). Neglecting the vertical flux term, we are left with:

$$\frac{\partial T}{\partial t} = -\mathbf{u} \cdot \nabla \mathbf{T} \implies ||\nabla \mathbf{T}|| \cos\theta = -\frac{1}{||\mathbf{u}||} \cdot \frac{\partial T}{\partial t}$$

where θ is the angle between $\mathbf{u}$ and $\nabla\mathbf{T}$. The quantity $||\nabla \mathbf{T}|| \cos\theta$ or the *along-current component of the gradient of temperature* (hereafter denoted $\nabla T_{||}$) will serve as our proxy for horizontal thermal gradients. For the question of whether this single component is of the same order as the full gradient, see Section 3.1.

The timescale chosen to differentiate T is daily—so a centred difference involves temperature data over three days. Consequently, if θ fluctuates significantly over the course of a two-day period, the value of $||\nabla \mathbf{T}|| \cos\theta$ is by definition meaningless. With respect to any compass direction (I chose the East), we can write $\theta = \theta_u - \theta_T$, where θ_u is the angle made by the current to the East. Then $d\theta_u/dt$ serves as a **quality flag** for us, and data are rejected when it is above a certain threshold (which I set to $40^\circ/\mathrm{day}$). We see in the figure below that some outlier values of $\nabla T_{||}$ are correlated with high values of this flag.

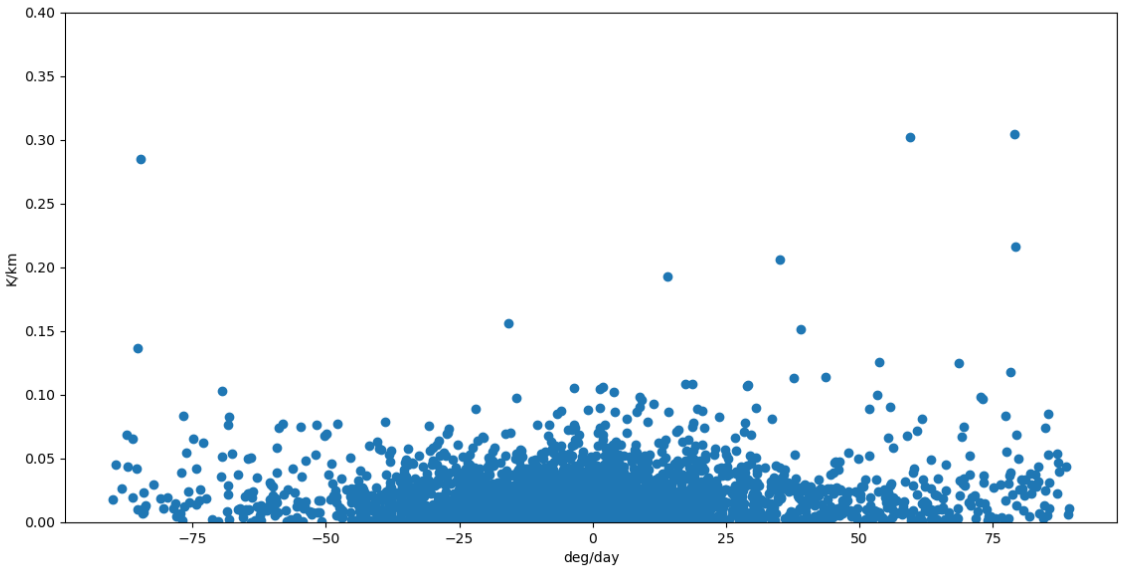

Figure 2.3: $\nabla T_{||}$ on the y-axis versus the current turning rate $d\theta/dt$ on the x-axis.

An attempt was made to "correct" for the factor of $\cos\theta$, by assuming $\nabla\mathbf{T}(z)$ to be parallel to the gradient of SST as calculated from MUR (JPL MUR MEaSUREs Project. 2015) data using the Belkin O'Reilly algorithm (Belkin et al., 2009) at all depths z. This assumption lead to inconsistencies in the data, such as ridiculously large values $\sim 5\ \mathrm{K\ km^{-1}}$. The assumption thus appears to be grossly wrong, with the thermal gradient at the very surface being poorly related to that at greater depths. A further limitation is that the MUR SST dataset is highly interpolated and smoothened (Chin et al., 2017), and may not represent well the finer-scale features detected by the mooring.

2.3 Accessing MetOp

As the mooring temperature data are limited to subsurface observations, I accessed SST data from the MetOp (OSI SAF (2016): Global L3C AVHRR Sea Surface Temperature (GHRSST)) satellites for the same period and location as that of the mooring, to complete our view of the entire profile. This dataset was chosen over MUR as it is derived from a single type of satellite-based instrument with no interpolation. In this dataset, the microwave radiance of sea surface (the "sub-skin" layer, with a depth of $\sim 1\ \mathrm{mm}$) is used to calculate a temperature at every pixel in a swathe covered by the satellite. The swathes are collated together on a grid of 0.05° latitudinal and longitudinal resolution, such that each grid point is observed at least once every 12 hours.

The data were downloaded from the Eumetsat Data Store (product name: Global L3C AVHRR Sea Surface Temperature, GHRSST) for the year of 2022. Thereafter, data during local night in the Mozambique Channel were selected as they are free of diurnal variation; accounting for the difference in time zones, these files were those with a UTC time index of 00:00:00 (midnight). Data were further selected to correspond to a latitudinal range of 20.03° to $29.97^\circ\mathrm{S}$, and a longitudinal index of 33.03° to $52^\circ\mathrm{E}$.

2.4 Accessing Model Data

The CROCO simulations used by *Sudre et al, 2023a* to study fronts in the Mozambique Channel at subsurface depths were accessed for the purposes of comparison with data from the mooring. The output

from the $\frac{1}{12}^\circ$-resolution model for the year of 2000 were accessed from monthly netCDF files. The Net CDF Operator tool `ncks` was used to extract temperature and current velocity outputs from a vertical cross-section around the mooring (3 grid points of latitude by 3 of longitude). The year 2000 was chosen because it had a similar ENSO index to the year of interest 2022, as shown with the monthwise indices (months $1-12$) for both years below (accessed via NOAA's Climate Prediction centre at https://origin.cpc.ncep.noaa.gov/products/analysis_monitoring/ensostuff/ONI_v5.php):

2000	-1.7	-1.4	-1.1	-0.8	-0.7	-0.6	-0.6	-0.5	-0.5	-0.6	-0.7	-0.7
2022	-1.0	-0.9	-1.0	-1.1	-1.0	-0.9	-0.8	-0.9	-1.0	-1.0	-0.9	-0.8

CROCO models employ a topography-following vertical coordinate (σ) with higher vertical resolution near the sea surface and bottom, with the result that two points at the same σ-level are not necessarily at the same physical depth. The model output was thus first converted columnwise to depth (z) levels; the temperature data were then interpolated for every water column onto a standard, uniformly spaced vertical grid. Further, the model output was on an Arakawa C-grid, but was converted for simplicity's sake into an *unstaggered* grid, by interpolating the velocities u, v, w at the grid centres, from the values known at the grid boundaries. This provided a comparable, simulated year-long dataset of temperatures and current velocities.

The model data thus allow us to directly calculate $\nabla \mathbf{T}$ as well as $\nabla T_{||}$, to compare them and to validate our use of this proxy against simulation results.

2.5 Statistical correlations

In this thesis, I examine the relationships between different variables using timeseries data. The simplest way to relate two variables $\mathbf{X}$ and $\mathbf{Y}$ involves two assumptions:

1. Allowing for some unbiased noise, the observations X_t and Y_t are **linearly related**.
$$Y_t = mX_t + c + \varepsilon_t$$
2. The noise term ε_t is independent and identically distributed across all times t. In particular, this means the conditional variance of $Y_t | X_t = x$ is the same for all x. (Assumption of homoskedasticity)

In other words, given a value x of X_t, we have a distribution for Y_t with mean $mx + c$ and variance given by $\operatorname{Var} \varepsilon_t$. (Note that an analogous statement hold for the distribution of X_t given $Y_t = y$.) With this model and our two timeseries, we can identify a best-fit line, passing through the mean value of Y for a given value of X. One way of quantifying the size of this effect is by looking at the value of m; but the noise ε_t means that many realisations of these variables may lie off the line, implying a weaker relationship. We thus need to use a metric like the goodness of fit, R^2, or the Pearson linear correlation coefficient r, which is given by:

$$r_{X,Y} = r_{Y,X} = \frac{\operatorname{Cov}(\mathbf{X}, \mathbf{Y})}{\sqrt{\operatorname{Var}(\mathbf{X}))\operatorname{Var}(\mathbf{Y}))}}$$

where $r \in [-1, 1]$. If $|r|$ is higher, then the fit is better (for the best *linear* fit, $R^2 = r^2$; this is not true for other models). The sign of r tells us whether a positive or negative value of m yields the best fit.

In this thesis I investigate variables with complicated relationships, usually violating the requirements of linearity and homoskedasticity. This often yields low values of r or R^2 ($|r| < 0.3$) for a linear regression. Nevertheless, the values of m calculated from such an analysis can be quite useful as an indication of a broadly stronger or weaker *mean* effect of X_t on Y_t.

If linearity is violated, we may wish to test the broader class of models

$$Y_t = f(X_t) \ \mid \ f \text{ is monotonic.}$$

using the Spearman rank correlation coefficient. We define $\text{rank } A_t = j$ such that there are exactly $(j-1)$ values in $\{A_1 \dots A_n\}$ that are less than A_t. Then, we can carry out a correlation analysis replacing $\mathbf{X}$ with $\text{rank } \mathbf{X}$ and $\mathbf{Y}$ with $\text{rank } \mathbf{Y}$. The resulting value

$$\rho_{X,Y} = \rho_{Y,X} = \frac{\text{Cov}(\text{rank } \mathbf{X}, \text{rank } \mathbf{Y})}{\sqrt{\text{Var}(\text{rank } \mathbf{X}))\text{Var}(\text{rank } \mathbf{Y}))}}$$

(where $\rho \in [-1, 1]$) generally examines the monotonic correlation. It can be greater than r, indicating a strong monotonic relationship that is nonlinear. However, it can also be less than r if the distributions for X_t, Y_t are strongly linear, except for small monotonic regions.

2.6 Comparing distributions

Continuing the foregoing discussion, if the dependent variable Y_t depends on the independent variable X_t, we expect a change in the conditional distribution (given by the probability density function) of Y, i.e, $\mathbb{Pr}\left(Y_t = y | X_t = x\right) \neq \mathbb{Pr}\left(Y_t = y\right)$. While regression may detect changes in the *central tendency*, other kinds of relationships might change the distribution of the outliers without changing the median or mode. In this case, the mean may respond to the presence of outliers, but it is then no longer a good stand-in for the central tendency.

One way to study this is to take two distinct ranges of $X-$ say, $[x_0, x_1],\ [x_2, x_3]-$ and then to compare the shape of the distributions, as histograms, of $\mathbb{Pr}\left(\ Y_t = y | X_t \in [x_0, x_1]\ \right)$ and $\mathbb{Pr}\left(\ Y_t = y | X_t \in [x_2, x_3]\ \right)$. This gives a visual look at the change in shape. Equivalently, we can use a quantile-quantile plot (hereafter "QQ plot"), which plots quantiles of one distribution ($\mathcal{D}_2-$ on the y-axis) against quantiles of another ($\mathcal{D}_1-$ on the x-axis).

If the distribution is identical or merely translated by a fixed value, the QQ plot follows a line parallel to $y = x$. If the line is steeper (less steep) the variance of $\mathcal{D}_2$ is less (more) than that of $\mathcal{D}_1$. $\mathcal{D}_2$ has more heavier tails than $\mathcal{D}_1$ if the QQ curve goes far below the $y = x$ on the left and/or above it on the right (indicating more extreme values than the original distribution). (Yearsley, 2024)

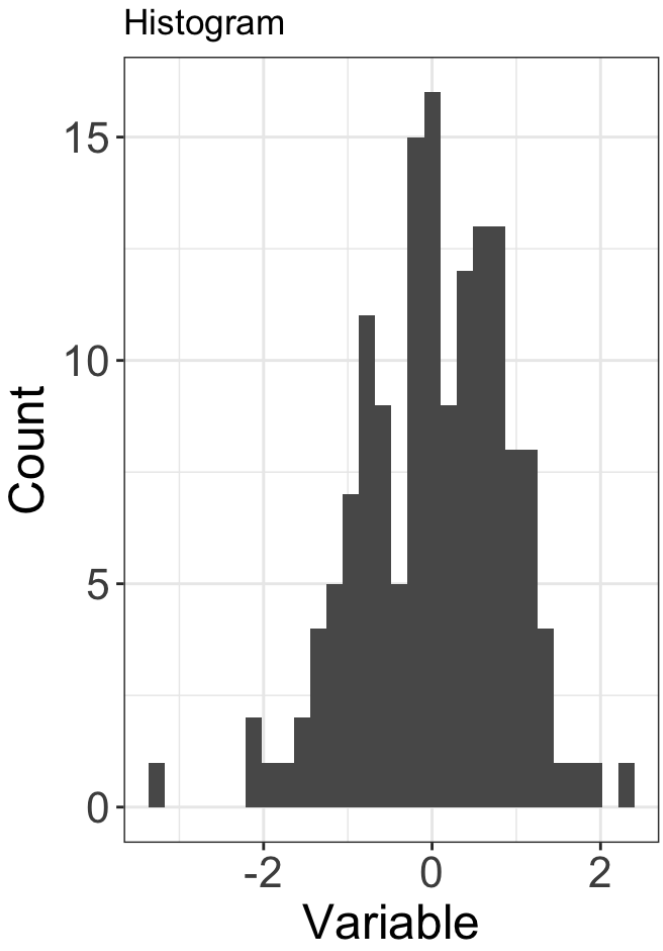
Histogram
Count
Variable
0
5
10
15
-2
0
2

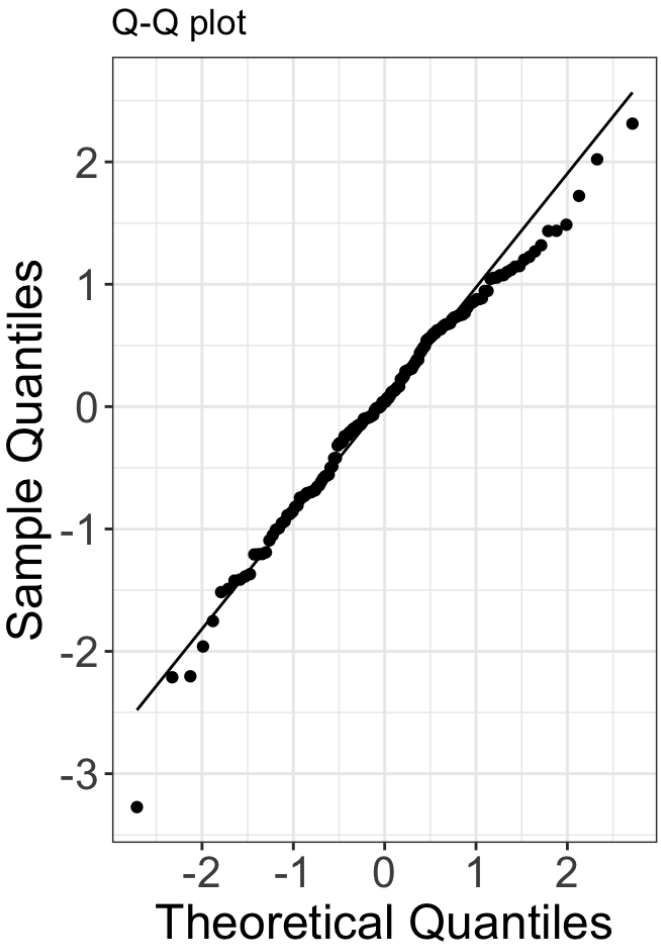
Q-Q plot
Sample Quantiles
Theoretical Quantiles
-3
-2
-1
0
1
2

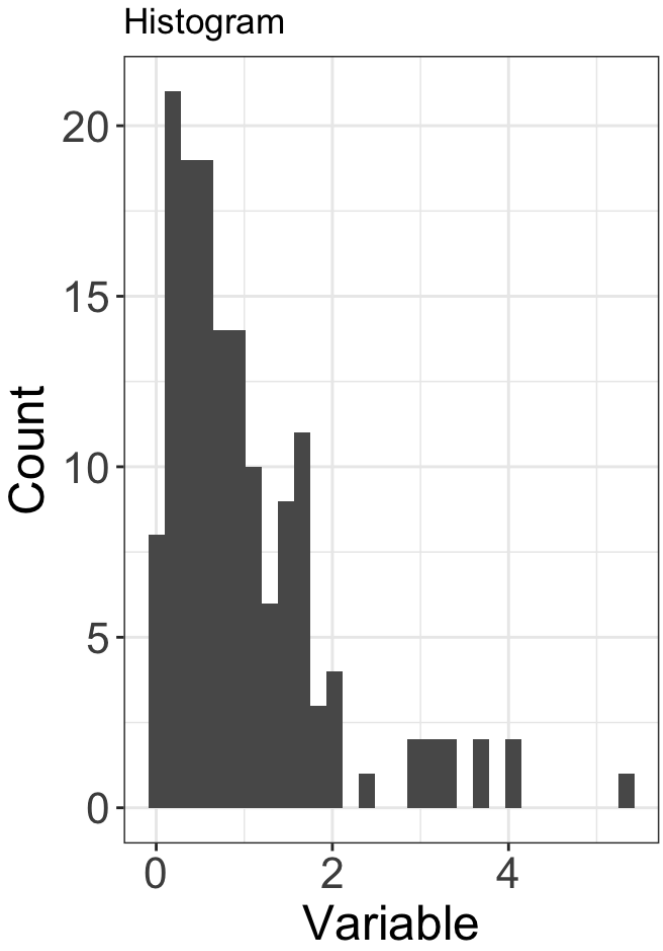
Histogram
Count
Variable
0
5
10
15
20
0
2
4

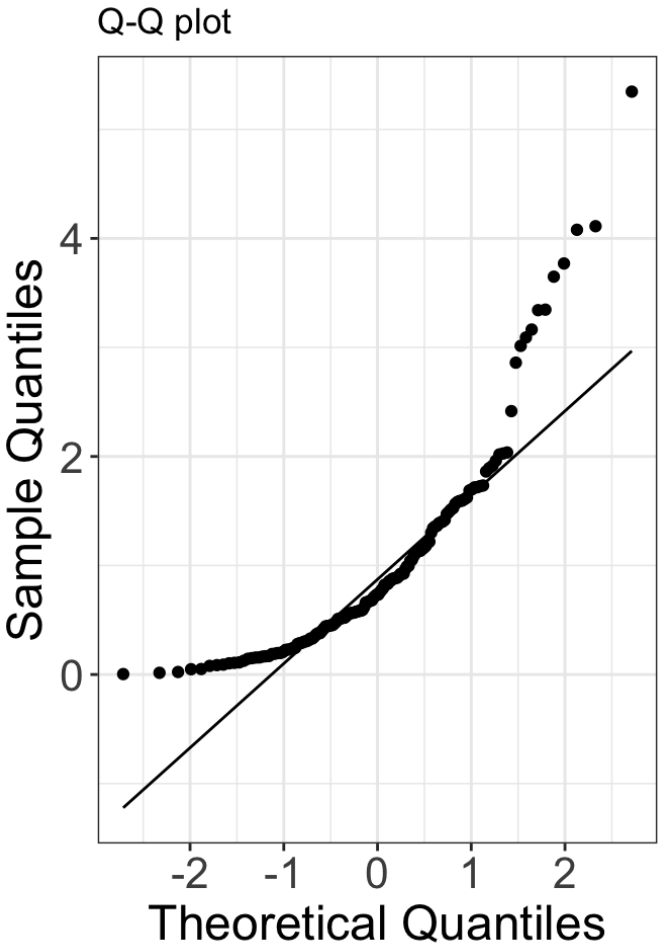
Q-Q plot
Sample Quantiles
Theoretical Quantiles
0
2
4
-2
-1
0
1
2

Fig 2.4: QQ plot of data versus a theoretical Gaussian distribution[14]: (top) where the data are distributed similar to the theoretical distribution; and (bottom) where the data are skewed to the left relative to that distribution

2.7 Spectral Method: Lomb-Scargle Periodogram

The Lomb-Scargle periodogram yields a spectrum for any timeseries, indicating the different dominant periodicities (VanderPlas, 2018). It can be understood as a plot of the least-squares goodness-of-fit for a sinusoidal model against the frequency of that sinusoid. It serves, thus, as a generalisation of the Fourier transform, without any phase information. Since we were interested in the submesoscale and finer-mesoscale phenomena, I filtered out lower-frequency components using a rolling window mean (window length = 30 days) on the original timeseries $(T, ||\mathbf{u}||)$. This was done by subtracting the smoothened timeseries from the original to retain only high-frequency components.

The frequencies for which the models were fit range from once in the entire time period up to the sampling frequency of 15 minutes. The effectiveness of the rolling window average was clearly visible as lower-frequency components did not show up in the periodogram. The method was implemented using the Python package `astropy`.

Results

3.1 Profiles of Temperature and Current Velocities

By interpolating measurements of T, u and v along the upper portion of the water column, we obtain timeseries of the vertical profiles of these variables (visualised below). The vertical range of this profile depends on the inclination of the mooring; under the action of strong currents, the mooring bends and the depths of the instruments change. Examples of such periods are in (e.g.) early May, early September and late September. The uppermost sensors (the CTD and the temperature recorder at $48\ \mathrm{m}$) face strong currents more often and consequently tend to be at an inclination most of the time. Sensor depths also varied at smaller timescales, such as under the influence of tides.

The temperature data reveal a seasonal cycle, with temperatures lowest in June-Sept highest in Oct-Dec (presumable they would continue to increase into Jan and Feb, but we lack data from that part of the year). The thermocline is sharpest ($\frac{\partial T}{\partial z}$ $\mathrm{is\ maximised}$) at a depth of $80 - 100\ \mathrm{m}$, which we use as a proxy for the base of the mixed layer.

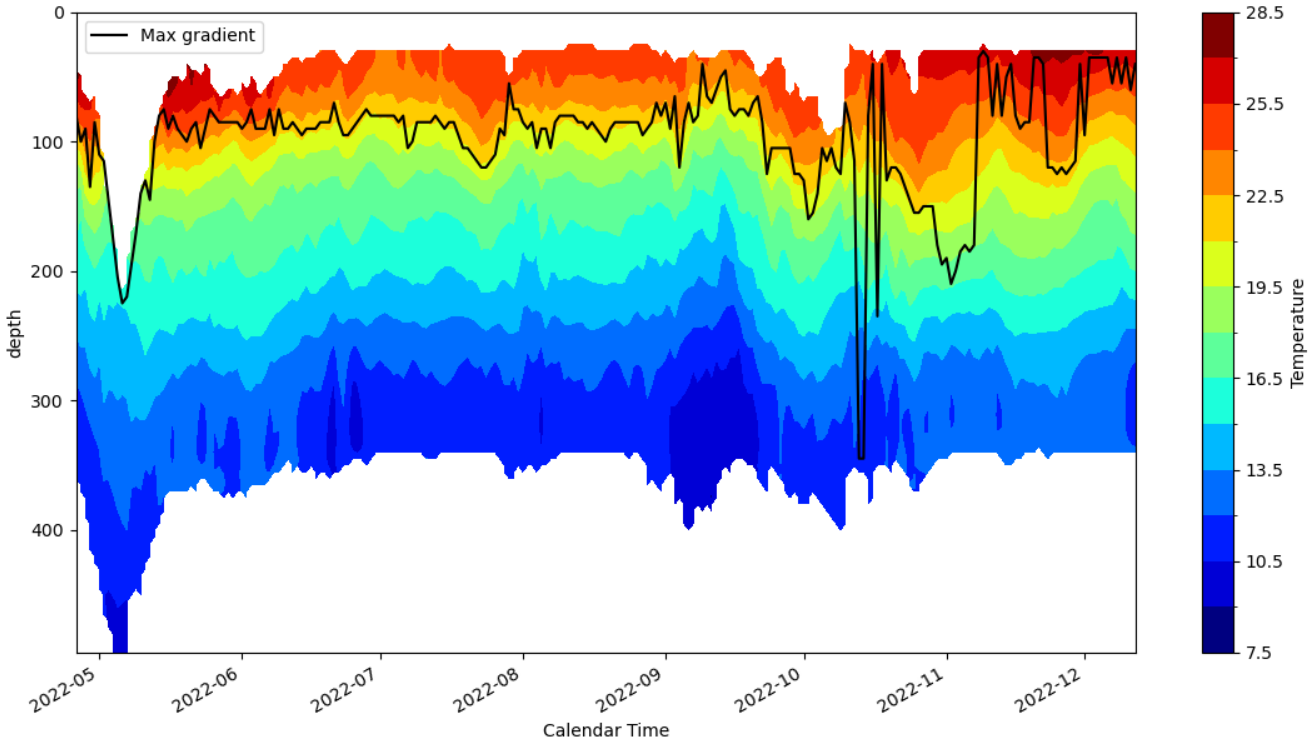

Fig 3.1: A filled contour plot of temperature plotted over depth and time. The location of the maximum vertical gradient of temperature $\partial T/\partial z$ is shown as the black line as a proxy for the mixed layer depth

The current velocity profiles $u(z)$, $v(z)$ are plotted in Fig 3.2. They are rather typical, with faster currents nearer the surface, and slower currents with increasing depth. The very erratic features near the surface are likely a composite of : (i) noise in the ADCP echo due to surface reflective effects and (ii) actual variability and strong wind-driven currents. Another noteworthy feature is the occasionally non-monotonic velocity profile; this is *a priori* concerning because the point of inflection was often near the position of the ADCP instrument itself, raising concerns as to whether it was an artifact of measurement, arising from the noisy cells near the instrument. In fact, discarding the first two cells ($\sim 10\ \mathrm{m}$) on either side and interpolating gives us the same kind of profile, indicating the points of inflection to be realistic.

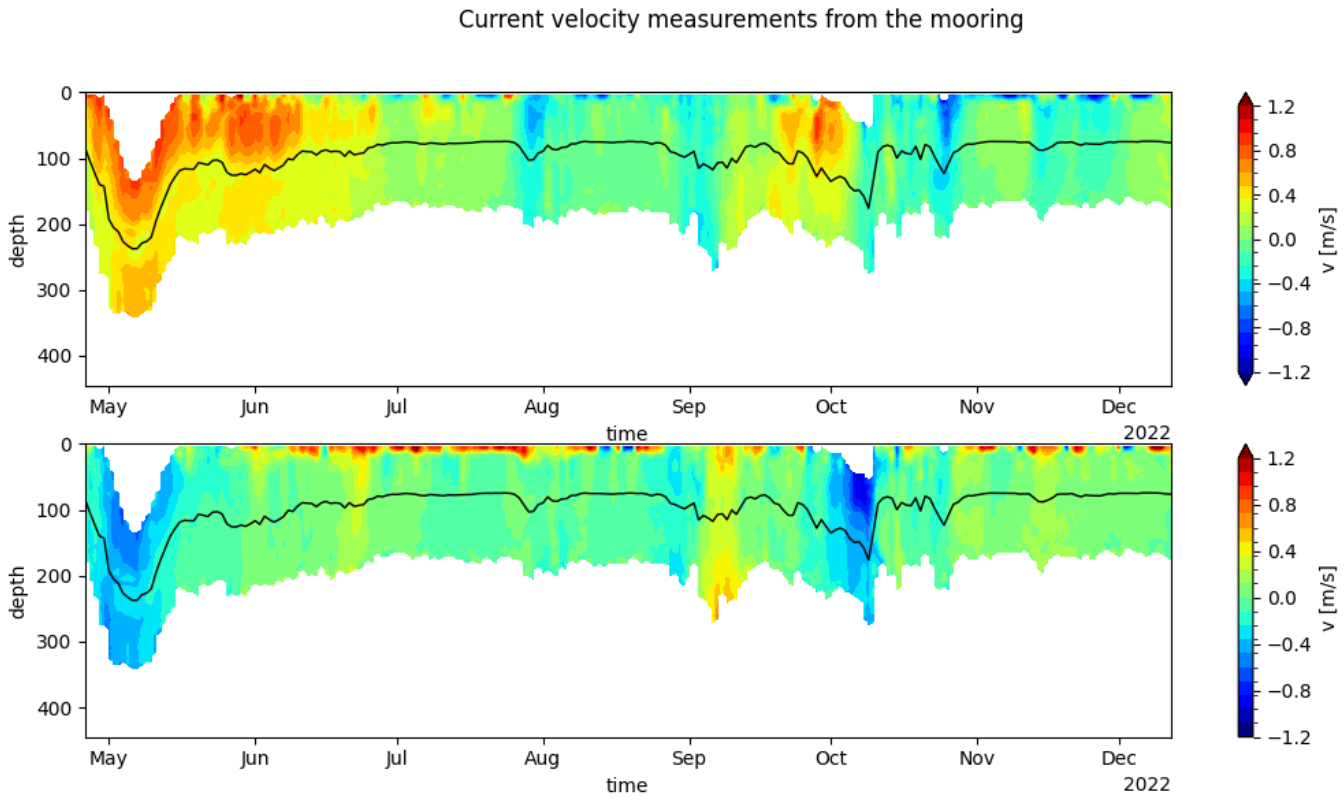

Fig 3.2: Filled contour plots of u (above) and v (below) over time and depth

To isolate submesoscale phenomena, we must check the spectrum of the quantities of interest. In other words, given a timeseries $T(z,t)$ we would like the corresponding frequency-spectrum function $\hat{T}(z,f)$ for all z (and likewise for u and v.) The spectra were filtered using a rolling window of 30 days (high-pass filter) visualised using a Lomb-Scargle periodogram at different depths, and are shown in Fig 3.3. Of note is the strong peak at $\text{period} = 1/f = \frac{1}{2}$ day, which we interpret as a tidal signature. Thereafter, we see signals with periods in the range of 2.5 to 10 days, that match the submesoscale timescales. An equivalent plot for the magnitude of the current velocity appears to be much smoother, except at 200 m depth, where the data are very sparsely sampled, leading to a nonrepresentative periodogram (not shown).

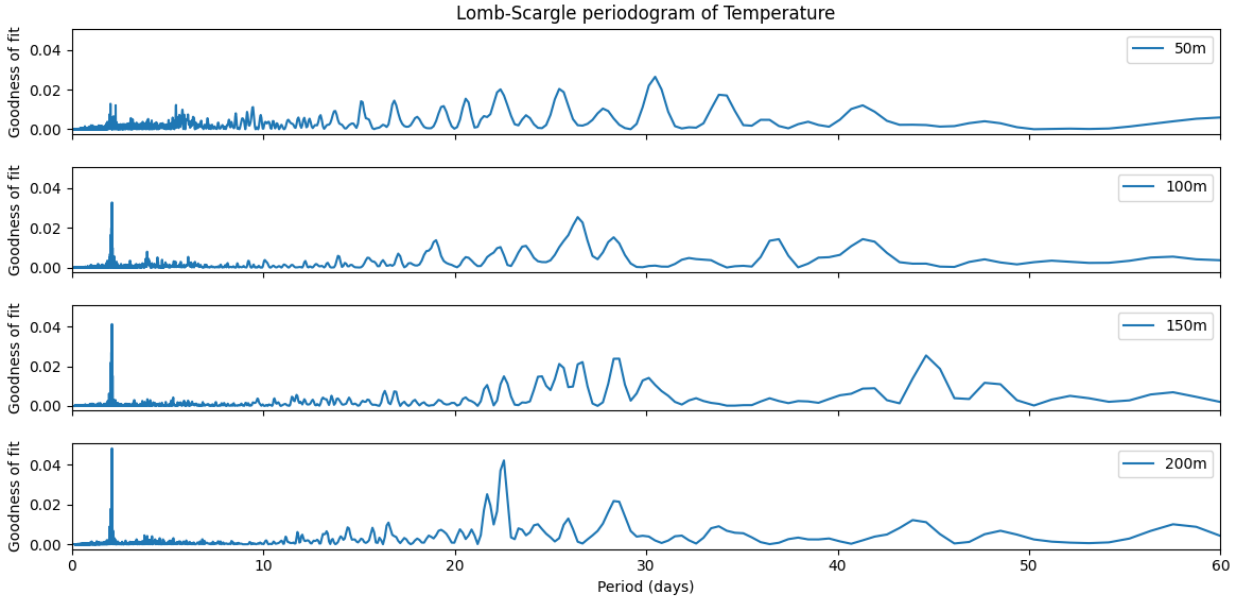

Fig 3.3: Lomb-Scargle periodograms of filtered (highpass filter by subtracting a rolling window average of

window length $30\ \mathrm{days}$, *hence with a maximum period of* $60\ \mathrm{days}$) *timeseries of temperature at depths* $50 - 300\ \mathrm{m}$. *Note the peak at* $12\ \mathrm{hours}$, *interpreted as a tidal signal.*

We wish to drop the smallest scales from this analysis, so as not to confuse frontal signatures with tides (and potentially, inertia-gravity waves). We therefore choose to degrade the resolution of our temperature dataset to a daily frequency, using daily temperature averages. Consequently, the alongcurrent gradient of temperature, calculated using centred differences to estimate dT/dt, depends on temperature over a 2-day period, and can only resolve well phenomena with a period greater than this. For current speeds of 20 to $30\ \mathrm{cm\ s^{-1}}$, this corresponds to a length scale of the order of $30\ \mathrm{km} -$ that is, the lower mesoscale/upper submesoscale.

3.2 Observations of fronts

A simple statistic of interest from these data is then the total number of fronts to pass by the mooring location during the period of deployment. The definition of a front as a local maximum in $||\nabla \mathbf{T}||$ is not relevant to Eulerian data from the mooring, and a contextual definition of "extreme" values of temperature gradient (substituted for by $\nabla T_{||}$) is instead employed. By extreme, I refer to values surpassing the 70 percentile threshold. This statistic I shall refer to as the *front count*.

Figure 3.4 is provided by courtesy of Floriane Sudre—a box-and-whisker plot showing different estimates of historical interannual variability in front counts. These front counts are derived either from the NOMAD dataset[1], for the period 2003-2020 (Sudre et al, 2023b) or from CROCO simulations (MOZ36_CR) at a spatial resolution of $\frac{1}{36}^\circ$ for the period 1993-2014. Also shown are the front counts from NOMAD in the years 2021 and (the year of the mooring observations) 2022, which are 72 and 65 respectively.

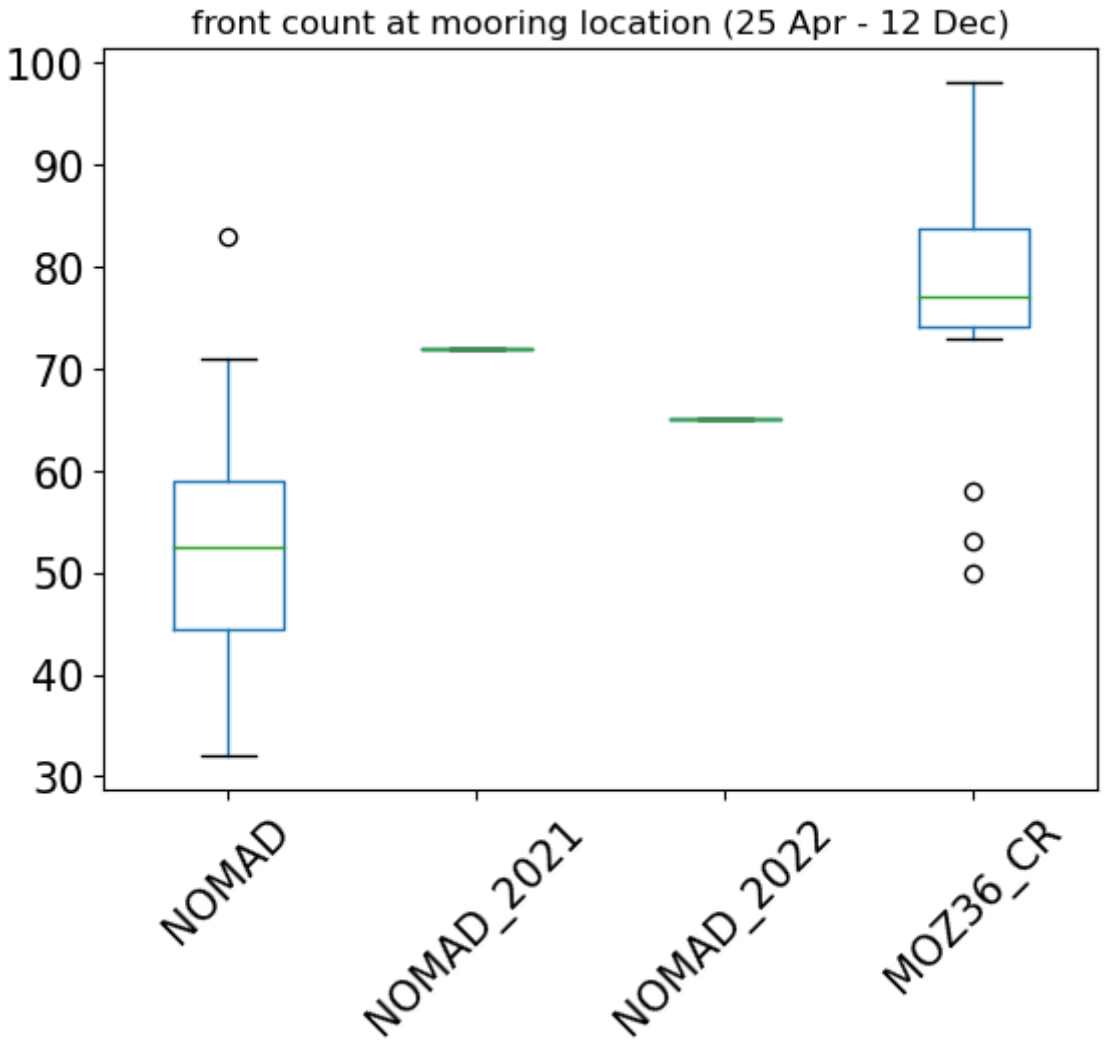

Fig 3.4: Box plots for front counts. The box extends from the Q1 to Q3 quartile values of the data, with a line at the median (Q2).
The whiskers extend from the edges of box to show the range of the data (1.5 times the interquartile range). Outliers are plotted as separate dots.
Threshold are chosen based on the 70th percentile value of the front intensity. For the simulations the threshold is computed from MOZ36_CR over the whole Mozambique Channel during 1993-2014 and is equal to 0.05°C/km (as in Sudre et al., 2023a). For NOMAD_2021 and NOMAD_2022, the threshold is computed over the EAFR (Longhurst ecoregion) during 2003-2020 and is 0.036°C/km (as in Sudre et al., 2023b).

Considering instead the mooring data, I provide in Fig 3.5 illustrative timeseries of the alongcurrent gradient (filtered against current turning rate) at depths of $70\ \mathrm{m}$, $80\ \mathrm{m}$ and $90\ \mathrm{m}$, as well as a mean across depths. Given the limited temporal coverage of this dataset, and the high interannual variability suggested in the previous figure, I have not used the $70\mathrm{th}$ percentile mark to set a front threshhold, but have instead made use of the threshholds arising from the datasets described above to generate front counts in Table 3.1.

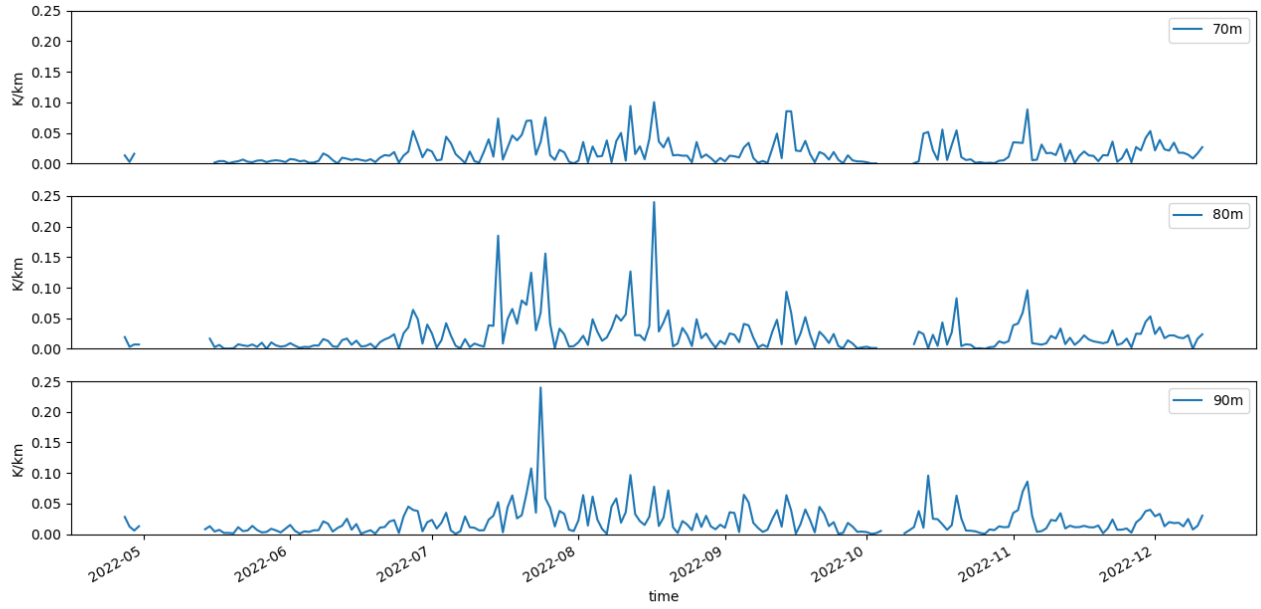

Fig 3.5: Timeseries of the alongcurrent thermal gradient $\nabla T_{||}$ at depths of $70,\ 80$ and 90 m.

Table 3.1: Front counts across different depths from the mooring

Depth	Total measurements	>0.036	>0.05
30	99	5	0
40	147	2	1
50	161	5	3
60	175	7	3
70	192	25	12
80	200	38	18
90	204	30	16
100	210	30	8
110	211	24	11
120	212	22	6
130	216	19	7
140	218	16	5
150	216	13	6
160	213	10	8
170	187	7	6
180	145	6	4
190	116	3	1
200	94	0	0

An immediately visible pattern from figure 3.5 is a *seasonal difference* between end April-mid July and Late July-December: the former season has very low frontal activity compared to the latter. This is coherent with the seasonal cycle described Sudre et al., 2023a for the South Mozambique Channel. This seasonal cycle appears to be confined to the subsurface layers, as SST data from both MUR and MetOp show no evidence of such a cycle, while mooring data indicate that one exists. Notably, the CROCO simulations do not distinguish between the surface and subsurface layers, predicting a seasonal cycle in both.

The variability in front count across depths is suggestive of variability in frontal activity along the water column, as described using CROCO simulation results in Sudre et al., 2023a. Reproduced below in figure 3.6 the time-mean vertical profile of the alongcurrent gradient of temperature from the mooring (2022) and an analogous profile for the full gradient from the simulations for the year 2000. The two are observed to be coherent in that they have a maximum at the base of the subsurface thermocline ($\sim 100\mathrm{m}$), but diverge in that the model predicts a slow decay of the gradient with depth (with an asymptote near $1\ \mathrm{km}$), where the mooring observes a fast decay by $300\ \mathrm{m}$ depth.

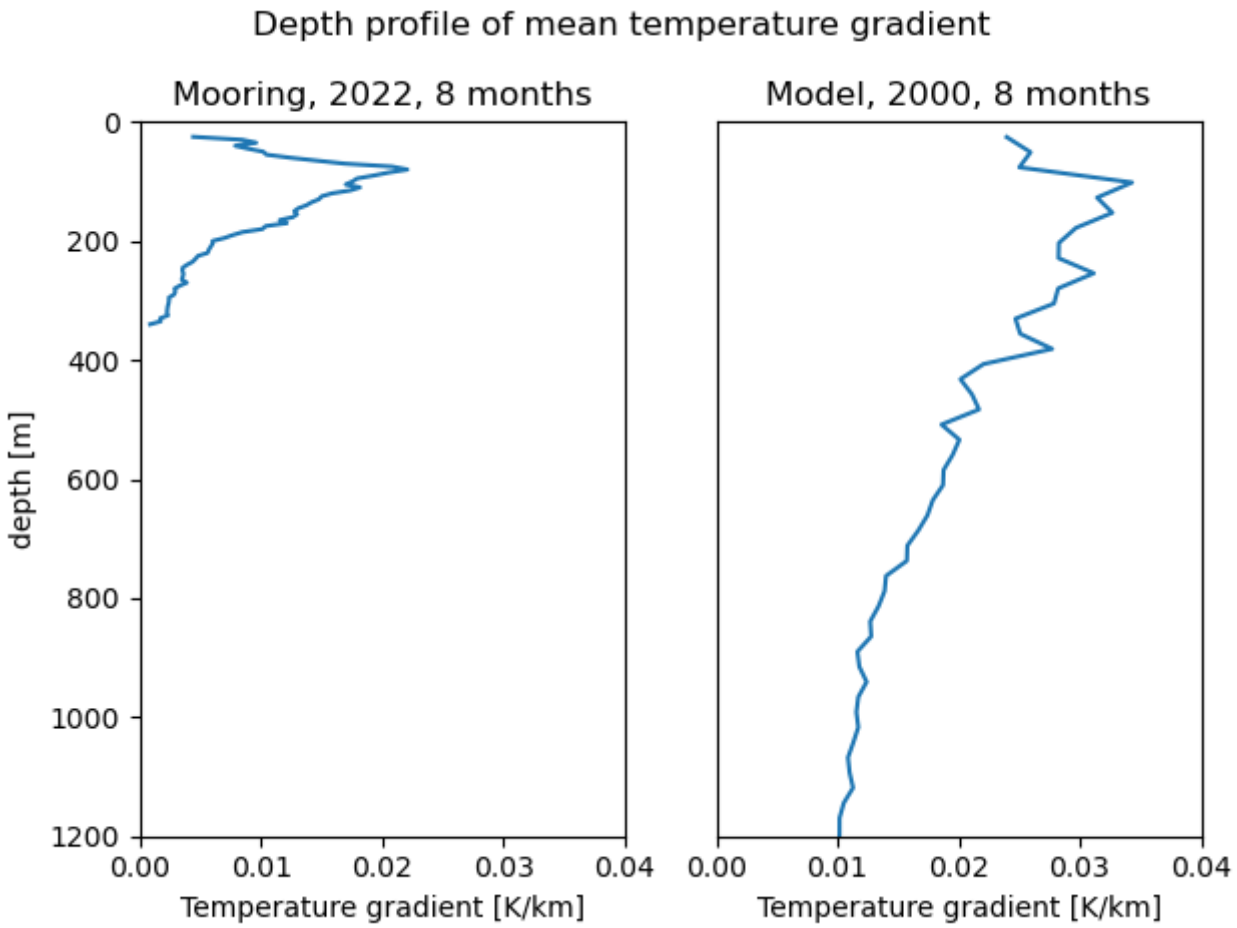

Fig 3.6: Comparison of vertical profiles of $\nabla T_{||}$ from the mooring and $||\nabla \mathbf{T}||$ from the CROCO run

Interestingly, this rapid decay might be a false signal, as we only have a few measurements of $||\mathbf{u}_h||$ at depths below $300\mathrm{m}$, resulting in a low sample size for data of $\nabla T_{||}$. I looked at the profile of the time-mean raw signal of $\partial T/\partial t$ (which has better coverage at those depths) and found a local minimum at $235\mathrm{m}$, below which it increases again. (shown in figure 3.7)

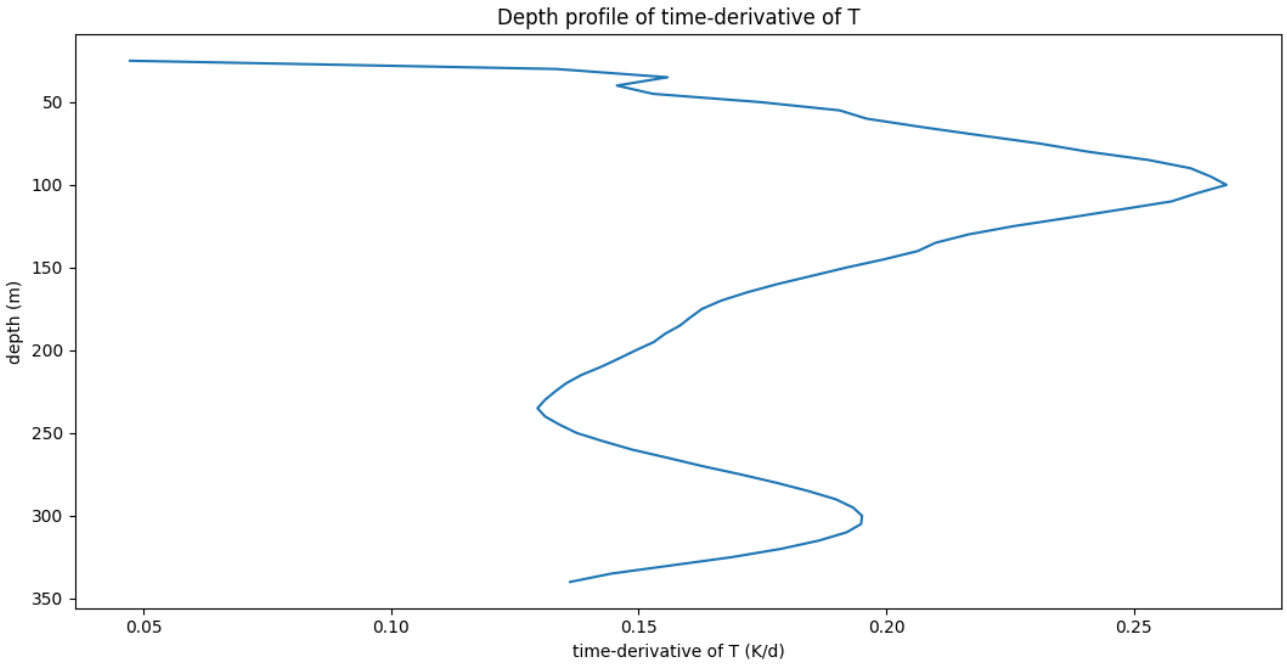

Fig 3.7: Time-mean vertical profile of $\partial T/\partial t$. Note that this quantity does not decay as sharply as $\nabla T_{||}$. As these data have better coverage, they cast doubt on the sharp decay marked in the profile of $\nabla T_{||}$. Note further that if $||\mathbf{u}_h||$ decreases with depth, the decay in $\nabla T_{||}$ will be slower than that in $\partial T/\partial t$.

Is this behaviour of subsurface fronts coherent with SST gradients observed from the surface? No significant correlation between the SST gradient at the mooring location (from MetOp) and the timeseries of $\nabla T_{||}$ is observed at any depth (Fig. 3.8). Nor does there appear to be a seasonal cycle in the SST gradient that matches that of the mooring or the model—a mismatch already remarked in Sudre et al, 2023a.

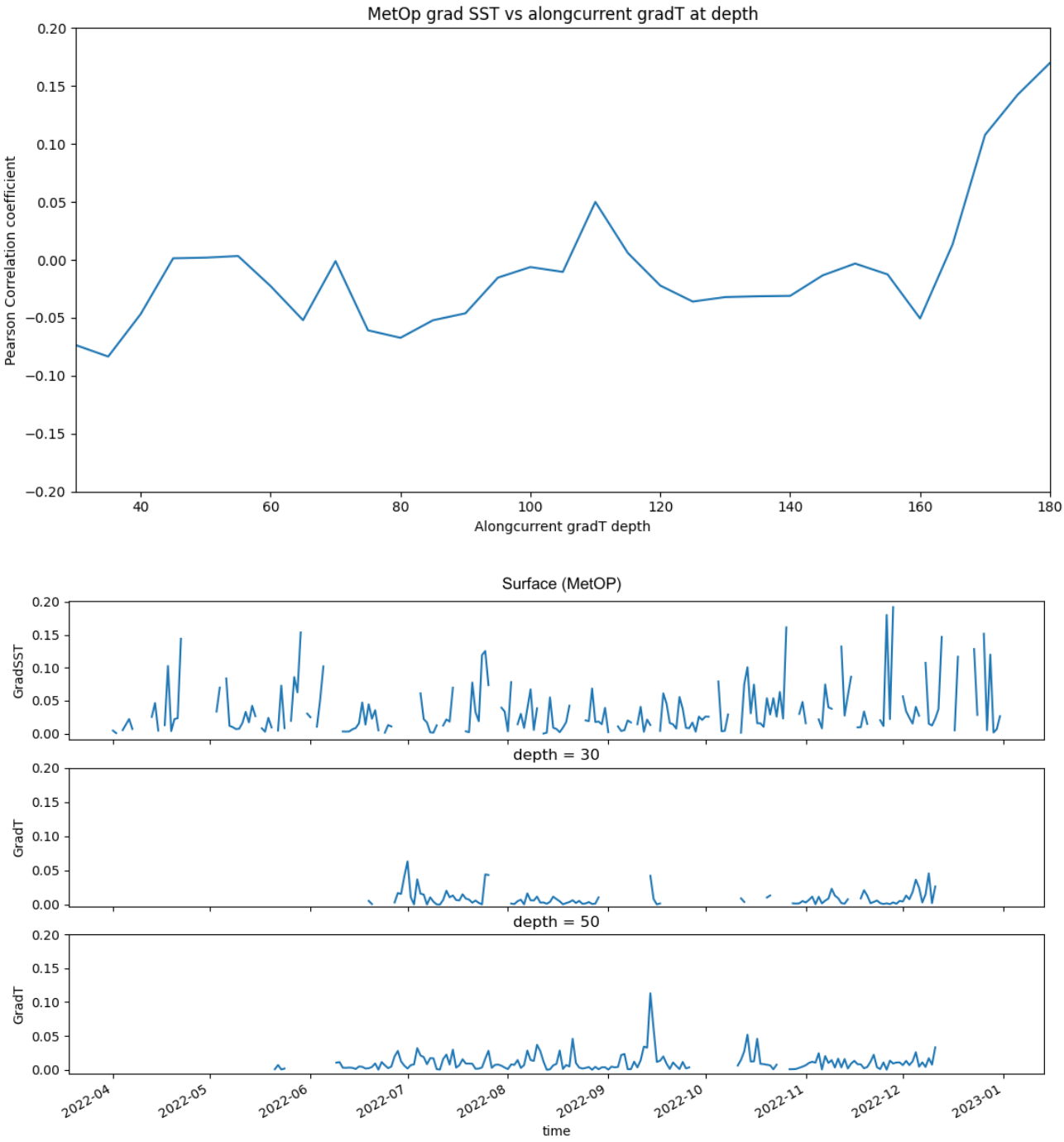

Fig 3.8: (top) Correlations between the gradient of MetOp-SST at the mooring location and $\nabla T_{||}$ along various depths and (bottom) Timeseries of grad SST (from MetOp) and $\nabla T_{||}$ at depths of $30\mathrm{m}$ and $50\mathrm{m}$

Given the variability across depths in time-mean frontal activity, it is meaningful to ask how coherent a front is across the water column—that is, is the alongcurrent thermal gradient on a given day correlated across *subsurface* depths? I attempt to visualise in figure 3.9 this relationship by plotting out the Pearson and Spearman correlation coefficients across depths, pairwise. To compute such a coefficient, we need simultaneous measurements of $\nabla T_{||}$ from both depths, which are very scarce for pairs of distant depths (eg: $300\mathrm{m}$ and $100\mathrm{m}$), as the ADCP usually samples one or the other. The logarithm $(\log_{10})$ of the number of suitable measurements is depicted alongside to aid the interpretation.

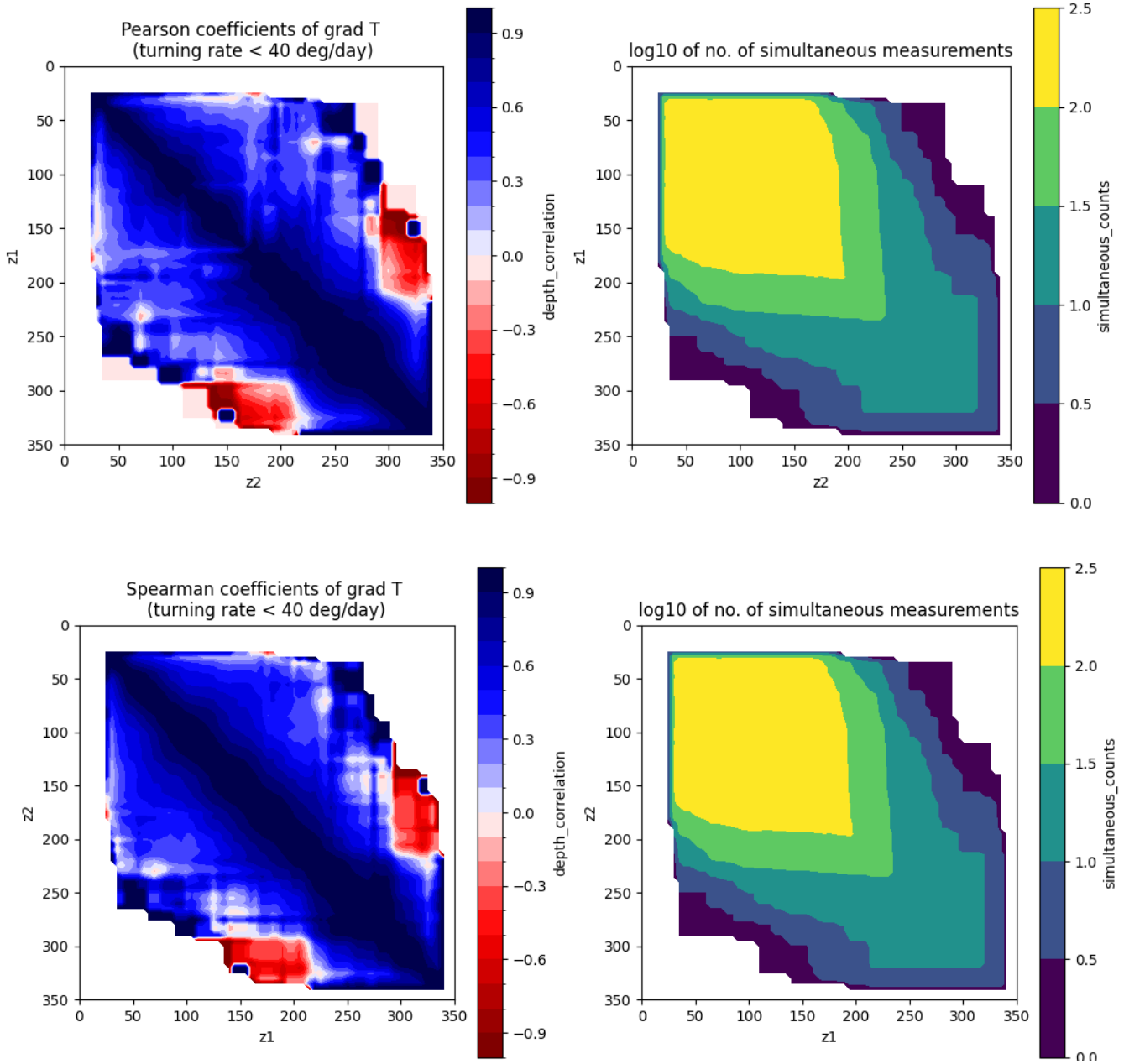

Fig 3.9: Visual representation of Pearson (above) and Spearman (below) correlation coefficients of $\nabla T_{||}\,(z1, z2)$ *on the left, accompanied by data on the availability of simultaneous measurements at both depths. Correlations are reliable when the number of such measurements are of the order of* 100*. See* §2.5.

Both correlation coefficients indicate mostly locally coherent behaviour where data are plentiful. The principal diagonal is mathematically required to be identically of value 1; the width of the "envelope" around the diagonal corresponds to how coherent frontal activity is around this depth. The fact that the envelope is widest at $100\mathrm{m}$ depth indicates that there is a strongly coherent frontal activity centred at this depth. The Pearson coefficient reveals a slightly more complicated story; there are local minima in the correlation values between neighbouring depths and $120\mathrm{m}$, and neighbouring depths and $170\mathrm{m}$. This might be indicative of two depth bands of frontal activity which are loosely coupled.

A histogram of depths corresponding to thermal gradient maxima (fig. 3.10) appears to confirm this simple story. It shows a trimodal distribution, with two broad peaks (at $80\mathrm{m}$ and $160\mathrm{m}$) and a short near-surface peak at around $50\mathrm{m}$. While the near-surface peak can be ascribed to surface-specific processes like mixed-layer

instabilities, the two lower peaks lack an obvious explanation. There is no evident seasonality to their distribution, so a simple deepening of the mixed layer does not appear a convincing explanation.

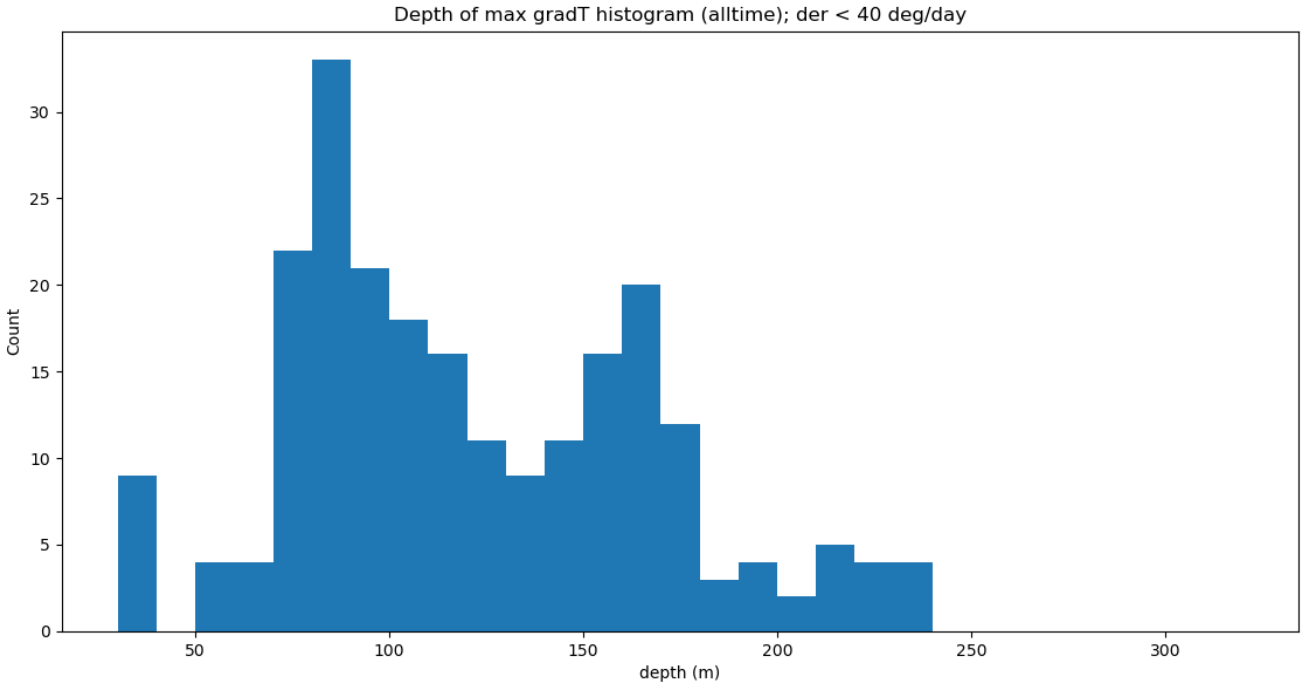

Fig 3.10: A histogram of the depths $z_m(t) \mid \nabla T_{||}(z_m) = \max\{\nabla T_{||}(z)\}$ *across different days*

A visualisation of the depth profiles of individual days confirms the diversity of front profiles. One peculiar observation is that the profile of $\nabla T_{||}$ is often non-monotonic on a *single* day, even taking strong values at two different depths but not in between them. Turning to $\partial T/\partial t$, which has greater spatial coverage, we note that an extremum often migrates along the water column over a few days; I interpret this as possibly indicative of an inclined frontal plane i.e., an offset across depths in the horizontal position of the gradient extremum. The timeseries from 20th to 24th August (Fig 3.11) shows how such a lag between lower and upper depths can give rise to two fronts in opposite directions at different depths; indeed this might be a representation of a dense filament.

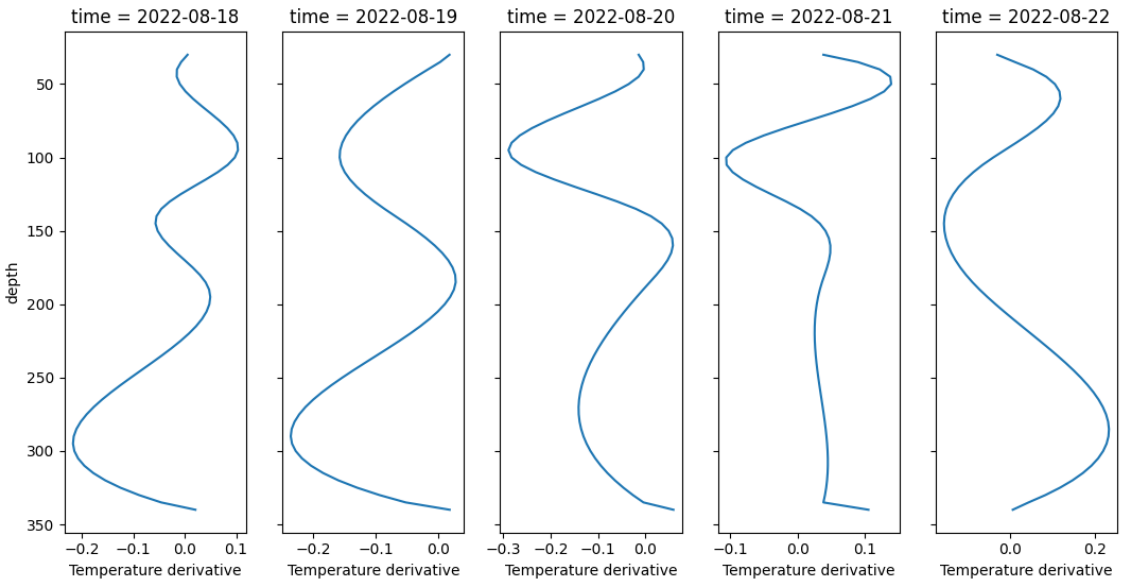

Fig 3.11 Profiles of $\partial T/\partial t$. on successive days.

3.3 Backscatter: the biological story

The ADCP backscatter S_v indicates scatterer abundance (including abiotic or dead scatterers, zooplankton and micronekton). Before we can examine the impact of fronts on the biological populations captured by this data, we need to describe some first-order observations from this dataset. Owing to the well-documented phenomenon of the *diel vertical migration* (Bandara et al., 2021), we have an *a priori* reason to investigate separately the behaviour of S_v at different times of day. Upon visual investigation, (see Fig 3.12) we find different bands of increased S_v at different depths.

Relatively "calm" stretches of time (during which the ADCP had minimal diel variation in depth) were chosen for this investigation. The following patterns were observed:

- At near-surface depths ($40 - 65\mathrm{m}$) abundances were maximised during the day, from $7\mathrm{h}$ to $20\mathrm{h}$; but on many days, this pattern was rather broken into two maxima, from $7\mathrm{h}$ to $10\mathrm{h}$, and again from $15\mathrm{h}$ to $20\mathrm{h}$. One of these may be present without the other
- From $65 - 85\mathrm{m}$, our data are sporadic, as the binned cells (noisy cells) from the ADCP tend to be in this depth range. The instrument also heaves up and down with the tides, so this range widens when tidal cycles are more intense. We do not attempt to describe these data.
- From about $90 - 120\mathrm{m}$, we observe a relatively high abundance in the time range $16\mathrm{h} - 3\mathrm{h}$, again separable into two peaks, from $16\mathrm{h} - 21\mathrm{h}$ and again from $23\mathrm{h} - 3\mathrm{h}$. These peaks appear to be wider in the winter months ($15\mathrm{h} - 4\mathrm{h}$ in July as opposed to $16\mathrm{h} - 3\mathrm{h}$ in November). The two peaks often overlap, making them hard to distinguish; yet one may be absent or present independently of the other.
- From 130 to $160\mathrm{m}$ there is a persistently high abundance (at all times of day).

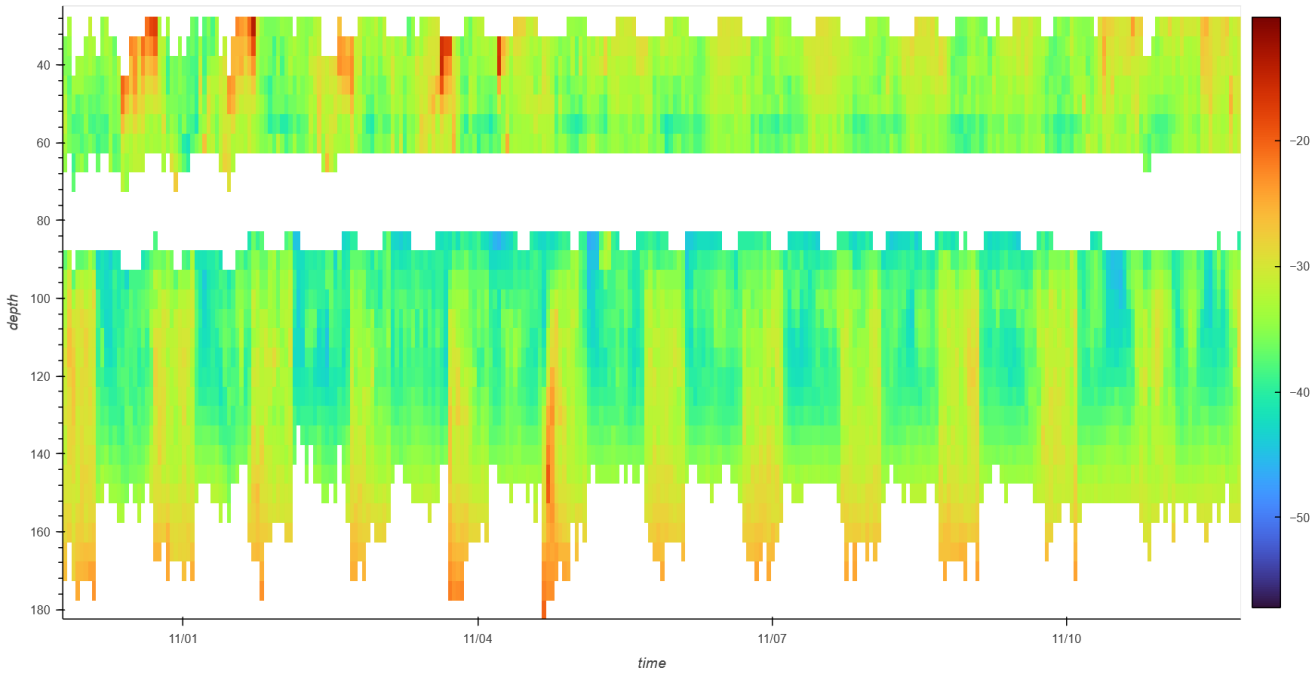
depth
40
60
80
100
120
140
160
180
11/01
11/04
11/07
11/10
time
−20
−30
−40
−50

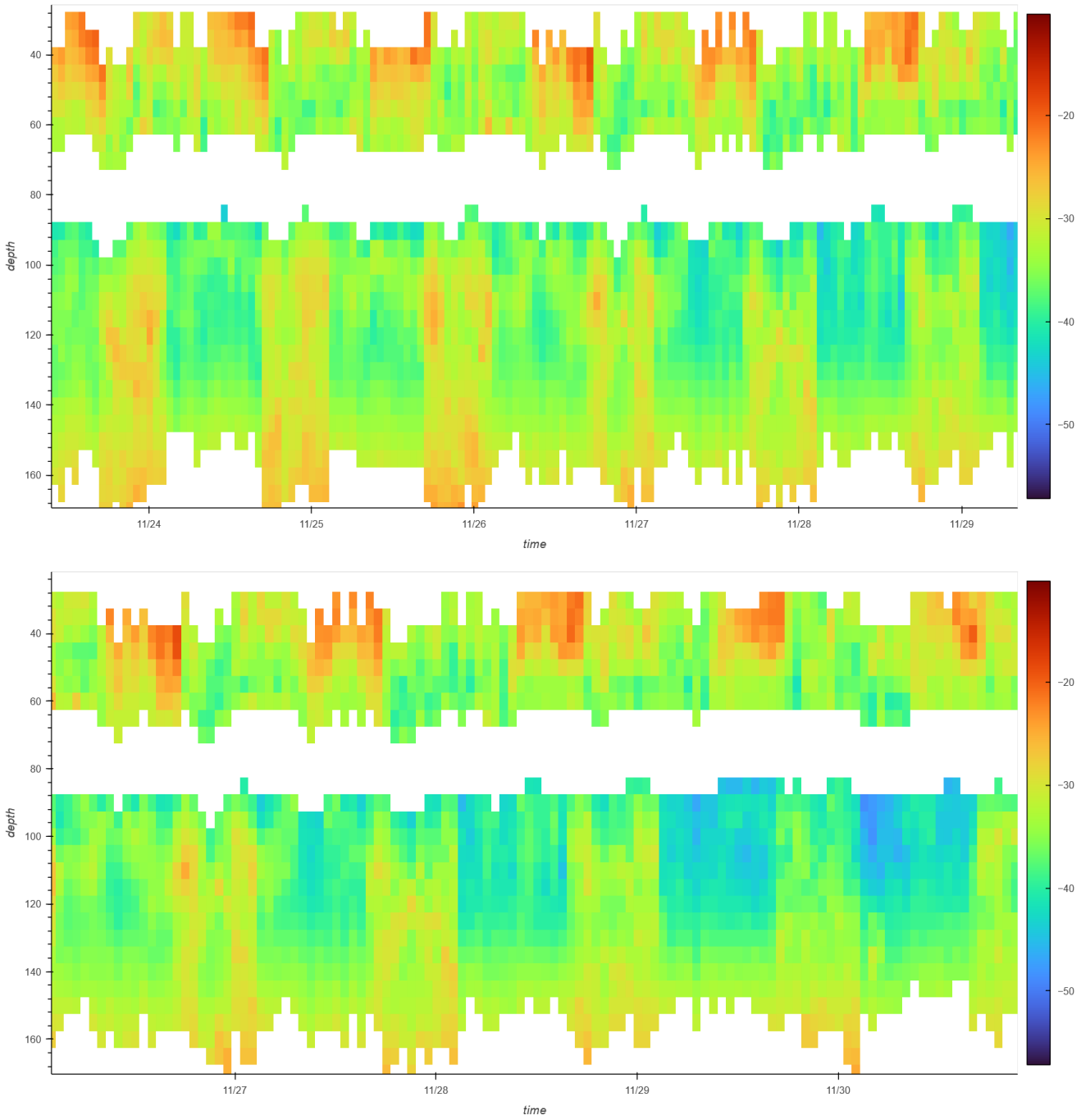

Fig 3.12: Plot of S_v over the depth range of the ADCP for different periods to typify the data, and highlight diel variations in upper and lower depths. Note the gap corresponding to ADCP binned cells. The topmost figure is a broad section showing typical variations on days with weak tidal variations. The other two demonstrate the variability in these features as well as some of the clearer bands.

3.4: The effect of fronts on scatterer abundance

The diel migration of zooplankton and micronekton allows, *a priori*, for non-local dependences on temperature gradients. Consider a population that migrates from depth z_1 at time of day t_1 to z_2 at t_2. Then the gradient of temperature at z_1 might be seen to have an impact at z_2 as well, at the appropriate time. I analysed the response of S_v in each specified depth and time range to $\nabla T_{||}$ in the same depth range, as well as elsewhere along the water column. Strong dependences were seen on the gradient of temperature at depths $100 - 200\mathrm{m}$.

The relationship between horizontal thermal gradients ($\nabla T_{||}$) and plankton abundance (S_v) is a complex non-linear one. By complex I mean that while the shape of the distribution of the latter depends on the value of the former, $\left[\mathbb{Pr}\left(S_v = a\right) \neq \mathbb{Pr}\left(S_v = a|\nabla T_{||} = b\right)\right]$, where $\mathbb{Pr}$ denotes a probability, this effect may not always show up as a strong shift in the *mean* of S_v as $\nabla T_{||}$ varies. Ordinary least squares regresssion may not be pick up these more subtle relationships. Moreover, the response, whether of the mean or something more sophisticated like the quantiles, is non-linear; so fitting a line is not a justifiable way to describe these data.

Instead, I demonstrate these relationships by comparing the histograms of *conditional distributions* of S_v, for different ranges of $\nabla T_{||}$ – denoted $\mathbb{Pr}\left(S_v = a|\nabla T_{||} \in (b_0, b_1)\right)$. The ranges were chosen to contain the lower, middle and upper third of the $\nabla T_{||}$ values–i.e, to be between the minimum and $\frac{1}{3}^{\text{rd}}$ quantile; the $\frac{1}{3}^{\text{rd}}$ and $\frac{2}{3}^{\text{rd}}$ quantiles; and the $\frac{2}{3}^{\text{rd}}$ quantile and the maximum. This analysis was carried out, first, with values of $\nabla T_{||}$ at 100m.

A strong positive dependence of S_v on $\nabla T_{||}$ is found for the lowest depth band $130 - 160\text{m}$, (eg: Fig 3.13) where at all times of day the whole distribution shifts to the right, and its width reduces, for the higher tertile ranges of $\nabla T_{||}$. A similar, but inverted and weaker, relationship is observed for the middle depth band $90 - 110\text{m}$, during the period $3\text{h} - 15\text{h}$, when the scatterer abundances are relatively low. During the day, when the typical abundances are higher, the distribution does not shift much; but the period $16\text{h} - 21\text{h}$ corresponds to a shrinking left tail and a growing right tail, witnessed by a flip in the skewness of the distribution. Such a clear signal is not seen for the period $23\text{h} - 3\text{h}$. These are summarised by the Q-Q plots in Fig 3.14 provided to compare the bottom tertile range with the top tertile rage for each case.

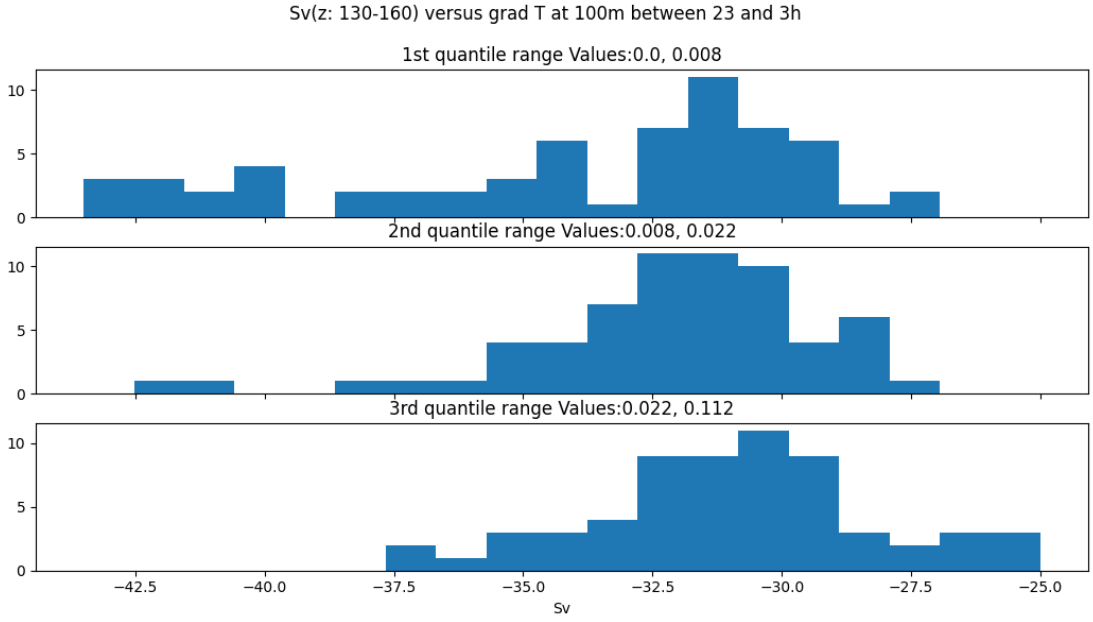

Fig 3.13: an example set of histograms (depths: $130 - 160\text{m}$, time of day: $23\text{h} - 3\text{h}$) of S_v for the three intertertile ranges of $\nabla T_{||}$.

Q-Q plot of Sv in lower and upper tertile ranges of 100m grad T at depths 40-65m

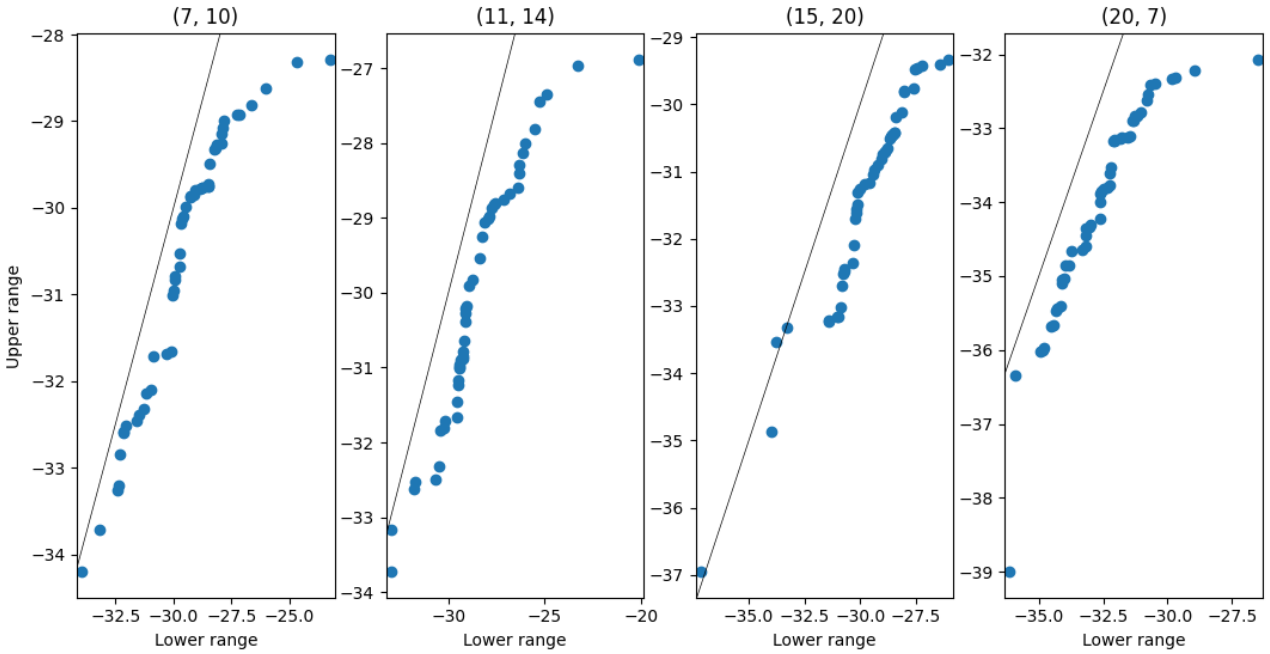

Q-Q plot of Sv in lower and upper tertile ranges of 100m grad T at depths 90-110m

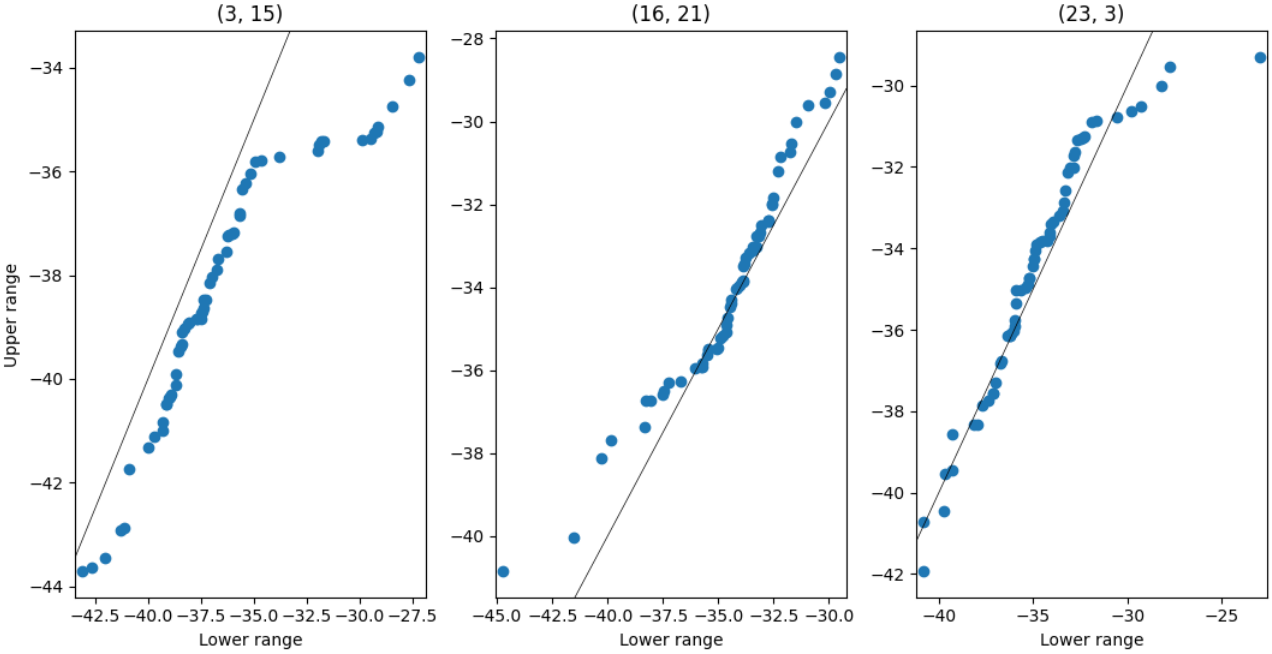

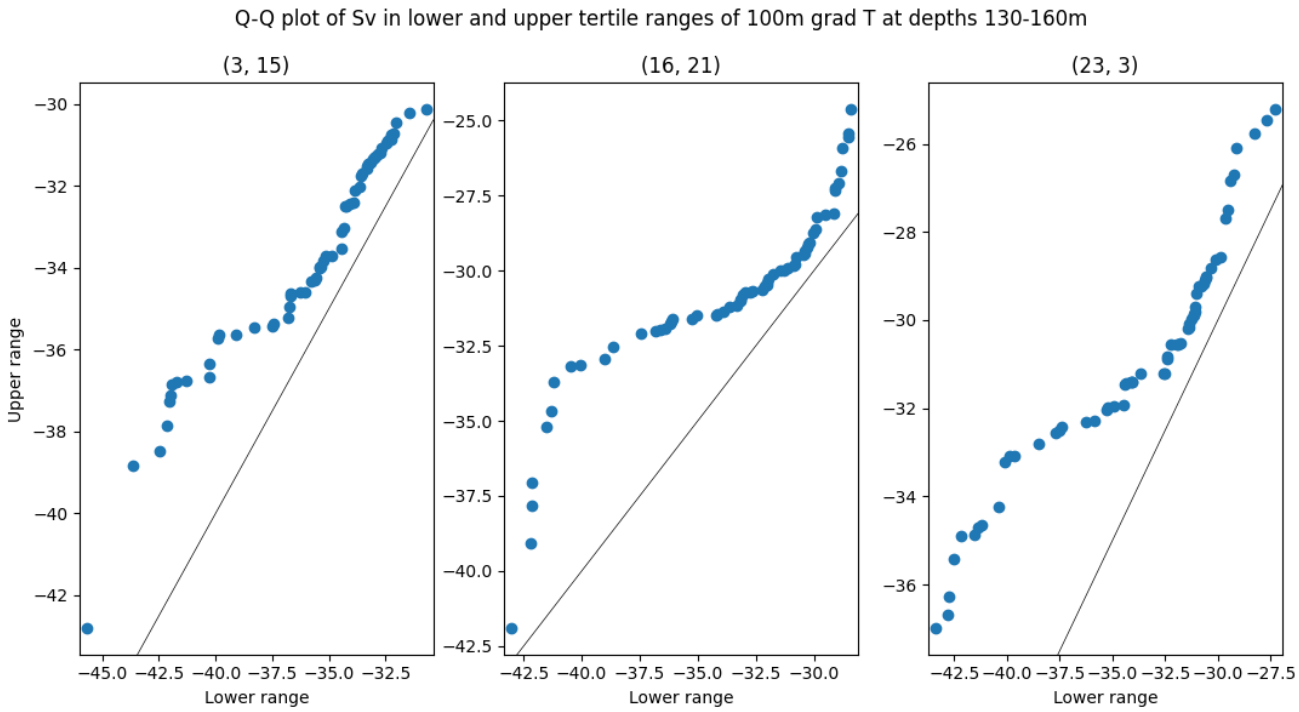

Fig 3.14: QQ-plots comparing the distributions of S_v for the highest (y-axis) and lowest (x-axis) intertertile ranges of $\nabla T_{||}$, at different time and depth bands.

What of the distribution of S_v at higher depths? The distribution has a much weaker response in terms of location (mean) and scale (variance) parameters, but during the time period $11\text{h} - 20\text{h}$ has a long right tail at low values of $\nabla T_{||}$, which nearly disappears at higher values, as shown by the skewness; this phenomenon reverses in the period $20\text{h} - 7\text{h}$ (appearance of a right tail) and disappears during $7\text{h} - 10\text{h}$. These effects are weak and less conclusive. A table of the statistical moments of the three intertertitle ranges for each case is provided below.

The thermal gradient at 40m was not found to have any strong correlations with the S_v values along the water column, while that at 150m has similar effects, but weaker ones at higher points along the water column.

Table 3.2: Moments of the conditional S_v distribution for the lower, middle and upper tertile ranges of $\nabla T_{||}$

Depth range	Hour range	Lower mean	Middle mean	Upper mean	Lower var	Middle var	Upper var	Lower skew	Middle skew	Upper skew
(40, 60)	(7, 10)	-29.488	-29.959	-29.936	4.258	6.572	4.149	0.377	0.172	0.165
(40, 60)	(11, 14)	-28.426	-29.071	-29.076	5.421	5.526	5.661	0.948	0.029	0.171
(40, 60)	(15, 20)	-29.686	-29.902	-30.671	3.907	5.118	4.028	-1.29	0.101	-0.171
(40, 60)	(20, 7)	-32.542	-32.941	-33.23	3.18	7.121	5.935	0.627	1.927	1.423
(90, 110)	(16, 21)	-34.479	-34.766	-33.945	7.575	10.141	6.499	-1.125	-0.344	-0.081

Depth range	Hour range	Lower mean	Middle mean	Upper mean	Lower var	Middle var	Upper var	Lower skew	Middle skew	Upper skew
(90, 110)	(23, 3)	-34.7	-35.486	-34.537	9.85	7.615	8.647	0.84	-0.261	-0.362
(90, 110)	(3, 15)	-36.35	-37.827	-38.228	14.315	7.958	6.47	0.781	1.097	-0.243
(130, 160)	(16, 21)	-33.607	-32.065	-30.768	17.508	11.922	9.325	-0.797	-0.516	-1.042
(130, 160)	(23, 3)	-34.014	-32.133	-30.916	19.237	7.891	7.085	-0.714	-1.158	-0.085
(130, 160)	(3, 15)	-35.897	-35.21	-33.708	12.478	8.283	6.595	-0.891	-0.6	-0.854

Conclusions

1. Observations of the gradient of temperature, reconstructed from mooring observations from 25th April 2022 to 12 December 2022, has a time-mean vertical profile peaking at around $100\mathrm{m}$ and decaying rapidly below. This is concomitant with Sudre et al 2023a's model results.
2. Further, a seasonal cycle is observed in the reconstructed gradient of temperature, with a peak in July and August. This, too, is concomitant with Sudre et al 2023a.
3. Correlations between subsurface thermal gradients and surface thermal gradients are weak.
4. Zooplankton and micronekton abundances (seen in ADCP acoustic backscatter) have a diel variation coherent with a reverse migration.
5. Subsurface thermal gradients (at near $100\mathrm{m}$) have demonstrable effects on zooplankton and micronekton abundances (acoustic backscatter) throughout the water columns, depending on time of day and depth. From 130 to $160\ \mathrm{m}$, there is a clear increase in abundances at all times of day. At other depths, the relationships are complex, dependent on the time of day, and changing the distribution of abundances without necessarily having a significant effect on the central tendency.

Discussion

4.1 Studying thermal gradients as a representation of fronts

Firstly, the impact of salinity is completely ignored in our identification of fronts. Consequently, we cannot determine *a priori* whether our reconstructed temperature gradients correspond to gradients in density (dynamically active) or to gradients in sea spice (dynamically inactive). One relevant piece of information comes from model data—the time-mean vertical profile of thermal gradients attains a maximum at the subsurface pycnocline, defined as the maximum of the Brunt-Väisälä frequency N (Sudre et al, 2023a) but this is furthermore concomitant with the maximum thermocline (maximum value of $\partial T/\partial z$) (Sudre, F.– personal communication). This has no bearing on the character of *individual* thermal fronts, but indicates that there is no gross mismatch between isopycnal and isothermal surfaces. Of course, the model does not represent certain smaller-scale features like freshwater inflow via rivers, so the representations of salinity are imperfect. Going forward, density fronts may make for a more theoretically justified object of investigation, requiring the use of CTDs at multiple depths (or, in the context of simulations, better resolved saline forcing).

Secondly, even if we identify intensified gradients in density, we are still ignoring half the picture: FSLEs. Density fronts drive a confluent circulation via geostrophy, but such circulations can be set up by other forces like wind stress. Furthermore, fronts with the same values of $\nabla\rho$ may *a priori* have different FSLEs, depending on the regional flow field in the vicinity of the front. Ultimately, it is this confluence that dictates the intensification of tracer gradients (density, nutrients, chlorophyll) and the passive aggregation of biota. NOMAD (Sudre et al., 2023b) is a dataset containing values of FSLEs (derived from a combined geostrophic and Ekman surface flow field) and thermal fronts for the Mozambique Channel and Mediterranean Sea. Once it is updated to include FSLEs for 2022, a timeseries of this parameter at the mooring location can be exploited as an alternate metric for fronts.

4.2 Alongcurrent gradient of temperature

The proxy $\nabla T_{||}$ is a transformed version of the metric $\partial T/\partial t$, which is all that can be extracted from a single mooring. Experiments with *mooring arrays* have previously been carried out and yielded measurements of submesoscale and mesoscale gradients—one needs at least three non-collinear moorings to extract a full gradient of temperature. One way forward is to implement a similar array experiment in the Mozambique Channel; another useful direction is to investigate whether my proxy correlates well with the full gradient in previous array-based studies. Array-based studies, however, confer the added advantage of being able to estimate w via the omega-equation (built on quasi-geostrophic theory) or by measuring the horizontal divergence and applying incompressibility: $w(z) = \int_0^z (\nabla \cdot \mathbf{u}_h) dz$.

$\nabla T_{||}$ measures the projection of $\nabla \mathbf{T}$ along the direction of the currents; assuming $\nabla \mathbf{T} \; || \; \nabla \rho$, and given that $\nabla \rho \; \perp \; \mathbf{u}_h$, we should expect the along-current component of both gradients to be negligible. However, as discussed in the Introduction, the submesoscale is not geostrophic to leading order. One way to verify this is to use the CROCO model output investigated by Sudre et al., 2023a to compare the magnitude of the full gradient and of its projection along the direction of the horizontal current. I did this, and found them to be of the same order of magnitude. If my proxy is a good estimate of this projection, then we have a quantity that correlates well with the true gradient, obtained from mooring data.

The CROCO $\frac{1}{36}^\circ$ model output does not however support a correlation between *my proxy* in terms of $\partial T/\partial t$ (in effect, what a mooring would observe in the model ocean) and the true projection $\nabla \mathbf{T} \cdot \hat{\mathbf{u}}_h$. Given the

smallness of the diabatic terms, I am inclined to attribute this discrepancy vertical advection (or to parameterised eddy diffusion at sub-grid scales). In other words, the local temperature tendency as a quantity would represent the *superposed* signals of upwelling/downwelling and horizontal fronts. The truth of this supposition will be verified by accessing w from the model output and inspecting how it correlates with $\partial T/\partial t$. I also intend to verify the scale-dependence of the importance of w, by investigating the parent CROCO $\frac{1}{12}^\circ$ model output for (hopefully) better correlations between my proxy and the true gradient. The reasons for this are twofold: (i) the scale of the coarser model is closer to the length scale I analysed from the mooring data; and (ii) I suspect that any vertical velocity due to internal waves will average out at large scales, and that even a quasi-geostrophic velocity w_{QG} might leave a smaller signal on $\partial T/\partial t$ over larger timescales as the water parcels tend to be restored to near their original depths. (In other words, I suspect the mean w over larger scales to be negligible).

If $\nabla T_{||}$ is explained almost entirely by w, it raises the question as to how to interpret the correlations we found between S_v and $\nabla T_{||}$, as well as the structure of the vertical profile of $\nabla T_{||}$ and $\partial T/\partial t$. At least for the biological data, the correlations found may remain meaningful, as correlations with w rather than with $||\nabla \mathbf{T}_h||$. From a mechanistic point of view, studying flow confluence (FSLEs) and vertical velocities as explanatory variables may be more justified, and future work may produce more interpretable results by focusing on these separately. Yet density/temperature gradients would remain of relevance, particularly near the surface, as they are visible to satellites and also easily studied in models (compared to FSLEs).

4.3 Observed properties of $\nabla T_{||}$

I now turn to a discussion of salient features from our observations: (i) the seasonality in $\nabla T_{||}$; (ii) the maximum it attains, below the mixed layer; and (iii) the shape of a typical vertical profile over the course of a few days.

The seasonal cycle described in Sudre et al 2023a has two peaks in a year, of which one appears to have been captured by the mooring. A year-long or multi-year experiment could result in a better description of this cycle. The mechanism behind this seasonality is unknown; while there is a seasonal signal in the simulated mesoscale EKE, it is much weaker. One possibility is that similar levels of mesoscale strain in different seasons have different "starting material"; that is, a season with higher levels of background temperature gradients will naturally have more intense gradients after frontogenesis. Two methods of testing this hypothesis are proposed: (i) to investigate the background (larger-scale) values of $||\nabla \mathbf{T}||$, from the CROCO $\frac{1}{12}^\circ$ and $\frac{1}{4}^\circ$ simulations; and (ii) to investigate FSLE data for seasonality. We anticipate that the seasonal variation of temperature gradients at fronts will be depend more strongly on that of background gradients if FSLEs show a weaker seasonality. The ultimate origins of this seasonality may then need to be traced to the Indian Ocean whence comes the water of the Mozambique Channel.

In the mooring data, both $\nabla T_{||}$ and $\partial T/\partial t$ attain a maximum at a depth of around $80 - 100\ \mathrm{m}$. As I explained in the introduction, this is then the depth at which isopycnal slope is steepest. A quasi-geostrophic balanced state (characteristic of the mesoscale) should restratify isopycnals (till their slope is of $\mathcal{O}(Ro)$) at scales smaller than the Rossby radius of deformation (~$100\ \mathrm{km}$); somehow, this process must fail for us to see the development of sharp submesoscale fronts.

Lévy et al.'s excellent 2012 paper "Bringing Physics to life at Submesoscale Fronts", presents an argument for surface-intensified fronts; briefly, as $\lim_{z\to 0^-} w = 0$, the tendency of fronts to restratify is most limited at surface. Without a vertical component of the circulation, they argue, frontogenesis (due to confluent

geostrophic flow and the ageostrophic assist of Hoskins, 1982) proceeds unchecked generating strong surface fronts. Thus they claim that fronts would be strongest at the surface, where there is frontogenesis without restratification. Sudre et al 2023a's CROCO simulations, on the other hand, would indicate that the fronts are most intense where N^2, and therefore presumably the restratifying flux $N^2 w$, are maximised.

This claim may be valid with respect to poor restratification; indeed, the lower stratification in the mixed layer N^2_{ML} also implies a smaller deformation radius, and can support higher isopycnal slopes. However, the very fact that the stratification is so low also implies that the horizontal gradient of density across such a slope would be negligible! On the other hand, frontogenesis is also a function of the existing horizontal gradients at mesoscale. While the density (or temperature) of the mixed layer may certainly vary horizontally, the spatial extent of such variation is limited; if a front forms within the ML (with isopycnals rising along the front), vertical mixing will act to cool the upper layer and warm the lower layer, thereby also weakening the front. In the thermocline, however, very slight variations in isopycnal slope can lead to strong gradients, and the frontogenic strain appears able to maintain such a front despite the tendency to restratify; such fronts were found by Johnston and Rudnik, 2009. Due to the same stratification, I do not interpret this maximum in $\nabla T_{||}$ as a maximum in w. The impact of the fronts on nutrient injections may thus be more complicated.

As to the time-mean vertical profile we observe, one mystery is the mismatch between the sharply decaying mooring-derived profile and the slow asymptote of the model at $\frac{1}{36}^\circ$. I do not have a ready explanation as to this difference, but would like to see if the difference persists at larger scales or if only very sharp fronts have a deep structure. Another possibility is that the signal from the mooring is more dominated by vertical advection than the horizontal gradients, and that such advection at thermocline depths has a strong impact that disappears in the more homogenously cool water below.

Of interest when we look at the daily profiles is the fact that they are often non-monotonic, and do not all peak at the same depth. First, let us cursorily discuss the existence of a few fronts that peak near the surface, or above the mixed-layer depth. Surface-specific mechanisms have been discussed in the literature, such as wind-assisted frontogenesis via Ekman convergence, Langmuir cells, or mixed-layer instabilities (MLI - the adiabatic restratification of the mixed layer, which leads to it "thinning" out while deeper isopycnals surface from beneath it)[7]. The lack of correlation between subsurface and surface gradients may substantiate the idea that different mechanisms dominate different depths. In fact, a subsurface front may not leave a strong SST signature, unless a cool isopycnal layer is able to outcrop up to the surface. The dynamics of such an outcropping, and the physics of how subsurface fronts may impact SST, is an interesting future direction for work.

What about the multiple subsurface peaks on certain days? These data, from July and August (when frontal activity is at an annual high) may represent successive fronts with lower depths lagging behind the upper depths. Consider again *Fig 1.1* and notice that the ageostrophic assist to frontogenesis is at the convergent locations, implying a *sloping* of the frontal axis, or rather implying that the site of maximum frontogenesis has a horizontal *offset* with depth. Whether this offset can be of the order of magnitude that appears to show up in these data $-\sim \mathcal{O}(10\ \mathrm{km})-$I am uncertain. Furthermore, the velocity shear with depth may also lead to a coherent frontal structure being sheared apart, with water from layers higher up arriving earlier at the mooring. Finally, submesoscale frontal activity can leave a residual signature of PV fluxed into the subsurface layers, circulating as *submesoscale coherent vortices* in the ocean interior (Thomas, 2008; McWilliams, 2016). It is quite possible that the signature of small eddies or SCVs dominated the signal of $\partial T/\partial t$ at greater depths.

4.4 S_v : the biological data

A quick look at the data of scatter abundance appear to show an interesting *inverse* vertical migration pattern, in which scatterer abundances increase during daytime in the near-surface band of $30 - 65$ m (though it is also possible that there is a downward migration of limited extent from the first $10 - 20$ m). In contrast, one of the windows of heightened biomass for the $90 - 120$ m vertical bands is from $23\text{h} - 3\text{h}$, which *could be* a case of the classic upward "midnight migration," from still lower depths; or it could be the same population which is near the surface at $15\text{h} - 20\text{h}$, now returning to lower depths for the night. Without observations of clear diagonals in the heatmap of the backscatter, and without data from our "hole" roughly in the range of $70 - 85$ m, we cannot infer the exact pattern of vertical migration. Moreover, we cannot classify the zooplankton into an echo class based on their reflective properties, as that requires measurements at multiple frequencies. Thus, for future work I would propose installing multiple ADCPs of different frequencies, lower in the water column (additionally giving us estimates of $\nabla T_{||}$ at greater depths) ideally giving us an uninterrupted view from the nutricline up to the surface and allowing us to detect different echo classes of scatterer. Note that there does not yet exist a method to infer taxonomic information from echo classes either, but it might help track distinct populations in their migration. Identifying populations, as well as calibrating a backscatter-to-biomass conversion, may be achieved by sampling the plankton in the vicinity of a mooring before recovering it, providing data for comparison.

Another matter to note is that the depth and time bands that I identified were basically the results of a visual analysis; that leaves an element of subjectivity. To make matters more objective, robust, and replicable, the use of wavelet analysis or another spectral method might be of greater utility. The timeseries are interrupted by `nan`s at certain depths when the mooring bends below them, so a simple multidimensional discrete Fourier transform will not work; though one may be used for periods during which the sampling is uniform. The Lomb-Scargle method from `astropy`, can be used to identify best-fit frequencies; but unlike the periodogram I generated for T and $||\mathbf{u}_h||$, the *phase* will be crucial to this analysis.

Before attributing the variations in S_v to $\nabla T_{||}$, it is important to verify that there is no direct relationship between S_v and T itself. While there is indeed a dependence on T, it operates on an interseasonal rather than daily timescale; hence I rule out the idea that the plankton populations are simply reacting to warmer/colder waters.

It remains for us to discuss explanations for the dependence of S_v on $\nabla T_{||}$. A variety of mechanisms by which submesoscale fronts can influence life have been reviewed in *Lévy et al, 2012*. Their main focus is the dual constraints of light and nutrients on primary productivity. Locally, vertical velocities associated with a front could make a deeper isopycnal rise into the euphotic layer, allowing for a nutrient injection from below the nutricline. Similarly, such an isopycnal slope would yield a locally small mixed-layer depth which may be less than that of the euphotic layer; in which case near-surface phytoplankton would no longer be vertically advected into low-light depths. Both of these effects reverse for the downwelling branch.

They also discuss the effect of the duration of the nutrient injection, pointing out that upwelling succeeded rapidly by downwelling may not leave the phytoplankton sufficient time for nutrient uptake, a problem that worsens for larger size classes of phytoplankton. Changes in primary productivity need to cascade up the food chain to affect higher trophic levels, and thus have smaller effects at those levels. They thus require a front to be active for a longer duration to have sustained local effects. However, they do not consider the question of *regenerated production*. If vertical currents advect marine snow into higher layers, it is possible that zooplankton will follow them. Such a mechanism would avoid the time lag due to one trophic level. I

propose to investigate this in my dataset by plotting the zooplankton abundances against the number of successive days of intense thermal gradients. A stronger correlation in this plot would then imply a mechanism with a time delay.

Unfortunately, the fluorimeter and hydrophones both failed, making it impossible to synthesise a story spanning all trophic levels at fronts from these data. Multiple trophic levels have to be accounted for, along with comptetion at each level, to fully explain the data collected in front transects. One previous study has noted that certain zooplankton can predate both heretrophic bacteria and phytoplankton. If a frontal ecosystem contains both phytoplankton and their predators, an increase in primary productivity may not show up as an enhanced chlorophyll filament from satellites; while the additional presence of another potential prey can reduce the predatory pressure and allow for sufficient increases in chlorophyll. Such interspecific interactions are hard to account for, and require coupled physical-biological models, resolving size classes, depths and running simulations with patchy initial conditions—an extension of the work figuring in *Lévy et al.*

References

1. Vallis, G K. 2005. Atmospheric and Oceanic Fluid Dynamics. Available from www.princeton.edu/gkv/aofd. Cambridge University Press.
2. Vanneste, J. “Balance and Spontaneous Wave Generation in Geophysical Flows.” *Annual Review of Fluid Mechanics*, vol. 45, no. 1, Jan. 2013, pp. 147–72. *DOI.org (Crossref)*, https://doi.org/10.1146/annurev-fluid-011212-140730
3. McWilliams, J. C. (2016). Submesoscale currents in the ocean. *Proceedings of the Royal Society A: Mathematical, Physical and Engineering Sciences*, *472*(2189), 20160117. https://doi.org/10.1098/rspa.2016.0117
4. Hoskins, B. J. (1982). The mathematical theory of frontogenesis. *Annual Review of Fluid Mechanics*, *14*(1), 131–151. https://doi.org/10.1146/annurev.fl.14.010182.001023
5. Mahadevan, A., & Tandon, A. (2006). An analysis of mechanisms for submesoscale vertical motion at ocean fronts. *Ocean Modelling*, *14*(3–4), 241–256. https://doi.org/10.1016/j.ocemod.2006.05.006
6. Samelson, R. M. (2013). Lagrangian motion, coherent structures, and lines of persistent material strain. *Annual Review of Marine Science*, *5*(1), 137–163. https://doi.org/10.1146/annurev-marine-120710-100819
7. Lévy, M., Franks, P. J. S., & Smith, K. S. (2018). The role of submesoscale currents in structuring marine ecosystems. *Nature Communications*, *9*(1), 4758. https://doi.org/10.1038/s41467-018-07059-3
8. Chin, L., & Young, W. R. (1995). Density compensated thermohaline gradients and diapycnal fluxes in the mixed layer. *Journal of Physical Oceanography*, *25*(12), 3064–3075. https://doi.org/10.1175/1520-0485(1995)025<3064:DCTGAD>2.0.CO;2
9. Tew Kai, E., Rossi, V., Sudre, J., Weimerskirch, H., Lopez, C., Hernandez-Garcia, E., Marsac, F., & Garçon, V. (2009). Top marine predators track Lagrangian coherent structures. *Proceedings of the National Academy of Sciences*, *106*(20), 8245–8250. https://doi.org/10.1073/pnas.0811034106
10. Sudre, F., Dewitte, B., Mazoyer, C., Garçon, V., Sudre, J., Penven, P., & Rossi, V. (2023). Spatial and seasonal variability of horizontal temperature fronts in the Mozambique Channel for both epipelagic and mesopelagic realms. *Frontiers in Marine Science*, *9*. https://www.frontiersin.org/articles/10.3389/fmars.2022.1045136
11. Brannigan L, Marshall DP, Naveira-Garabato A, Nurser AJG. 2015 The seasonal cycle of submesoscale flows. **Ocean Model.** ****92****, 69–84. (doi:10.1016/j.ocemod.2015.05.002) Crossref, ISI, Google Schola
12. Gordon, R. L. (1996). *Acoustic Doppler Current Profiler Principles of Operation: A Practical Primer* (P/N 951-6069-00), Second Edition. RD Instruments
13. Lentz, S. J., Kirincich, A., & Plueddemann, A. J. (2022). A Note on the Depth of Sidelobe Contamination in Acoustic Doppler Current Profiles. *Journal of Atmospheric and Oceanic Technology*, *39*(1), 31-35. https://doi.org/10.1175/JTECH-D-21-0075.1
14. K. L. Deines, "Backscatter estimation using Broadband acoustic Doppler current profilers," *Proceedings of the IEEE Sixth Working Conference on Current Measurement (Cat. No.99CH36331)*, San Diego, CA, USA, 1999, pp. 249-253, doi: 10.1109/CCM.1999.755249
15. Francois, R. E., and G. R. Garrison. “Sound Absorption Based on Ocean Measurements. Part II: Boric Acid Contribution and Equation for Total Absorption.” *The Journal of the Acoustical Society of America*, vol. 72, no. 6, Dec. 1982, pp. 1879–90. *DOI.org (Crossref)*, https://doi.org/10.1121/1.388673.
16. Flagg, Charles N., and Sharon L. Smith. “On the Use of the Acoustic Doppler Current Profiler to Measure Zooplankton Abundance.” *Deep Sea Research Part A. Oceanographic Research Papers*, vol.

36, no. 3, Mar. 1989, pp. 455–74. *DOI.org (Crossref)*, https://doi.org/10.1016/0198-0149(89)90047-2.

17. Wild, M., Folini, D., Hakuba, M.Z. *et al.* The energy balance over land and oceans: an assessment based on direct observations and CMIP5 climate models. *Clim Dyn* **44**, 3393–3429 (2015). https://doi.org/10.1007/s00382-014-2430-z
18. Comby, Caroline, et al. “Measuring Vertical Velocities with ADCPs in Low-Energy Ocean.” *Journal of Atmospheric and Oceanic Technology*, vol. 39, no. 11, Nov. 2022, pp. 1669–84. *DOI.org (Crossref)*, https://doi.org/10.1175/JTECH-D-21-0180.1.
19. Vélez-Belchí, Pedro, and Joaquín Tintoré. “Vertical Velocities at an Ocean Front.” *Scientia Marina*, vol. 65, no. S1, July 2001, pp. 291–300. *DOI.org (Crossref)*, https://doi.org/10.3989/scimar.2001.65s1291.
20. JPL MUR MEaSUREs Project. 2015. GHRSST Level 4 MUR Global Foundation Sea Surface Temperature Analysis. Ver. 4.1. PO.DAAC, CA, USA.
21. Belkin I. M., O’Reilly J. E. (2009). An algorithm for oceanic front detection in chlorophyll and sst satellite imagery. *J. Mar. Syst.* 78, 319–326. doi: 10.1016/j.jmarsys.2008.11.018
22. Chin, T.M, J. Vazquez-Cuervo, and E.M. Armstrong. 2017. A multi-scale high-resolution analysis of global sea surface temperature, Remote Sensing of Environment , 200 . https://doi.org/10.1016/j.rse.2017.07.029
23. OSI SAF (2016): Global L3C AVHRR Sea Surface Temperature (GHRSST) - Metop, EUMETSAT SAF on Ocean and Sea Ice, DOI: 10.15770/EUM_SAF_OSI_NRT_2011. http://doi.org/10.15770/EUM_SAF_OSI_NRT_2011
24. Yearsley, Jon. *Quantile-Quantile Plots*. 1 Jan. 2024, https://www.ucd.ie/ecomodel/Resources/QQplots_WebVersion.html.
25. VanderPlas, Jacob T. “Understanding the Lomb–Scargle Periodogram.” *The Astrophysical Journal Supplement Series*, vol. 236, no. 1, May 2018, p. 16. *DOI.org (Crossref)*, https://doi.org/10.3847/1538-4365/aab766.
26. Sudre, F., Hernández-Carrasco, I., Mazoyer, C., Sudre, J., Dewitte, B., Garçon, V., & Rossi, V. (2023). An ocean front dataset for the Mediterranean sea and southwest Indian ocean. *Scientific Data*, *10*(1), 730. https://doi.org/10.1038/s41597-023-02615-z
27. Bandara, K., Varpe, Ø., Wijewardene, L., Tverberg, V., & Eiane, K. (2021). Two hundred years of zooplankton vertical migration research. *Biological Reviews*, *96*(4), 1547–1589. https://doi.org/10.1111/brv.12715
28. Sudre, F. (Personal communication, PhD defense presentation, March 14 2024)
29. Lévy, M., Ferrari, R., Franks, P. J. S., Martin, A. P., & Rivière, P. (2012). Bringing physics to life at the submesoscale. *Geophysical Research Letters*, *39*(14), 2012GL052756. https://doi.org/10.1029/2012GL052756
30. Johnston, T. M. S., & Rudnick, D. L. (2009). Observations of the transition layer. *Journal of Physical Oceanography*, *39*(3), 780–797. https://doi.org/10.1175/2008JPO3824.1
31. Callies, J., Flierl, G., Ferrari, R., & Fox-Kemper, B. (2016). The role of mixed-layer instabilities in submesoscale turbulence. *Journal of Fluid Mechanics*, *788*, 5–41. https://doi.org/10.1017/jfm.2015.700
32. Thomas, L. N., Tandon, A., & Mahadevan, A. (2008). Submesoscale processes and dynamics. *Ocean modeling in an Eddying Regime*, *177*, 17-38.